2023-09

INVESTIGATION OF CYCLOTRON RADIATION FROM GRAPHENE-BASED DEVICES

Planillo, Jordan

Monterey, CA; Naval Postgraduate School

NAVAL POSTGRADUATE SCHOOL

MONTEREY, CALIFORNIA

DISSERTATION

INVESTIGATION OF CYCLOTRON RADIATION FROM GRAPHENE-BASED DEVICES

by

Jordan Planillo

September 2023

Dissertation Supervisor: Fabio Durante Pereira Alves

THIS PAGE INTENTIONALLY LEFT BLANK

REPORT DOCUMENTATION PAGE	*Form Approved OMB No. 0704-0188*

1. AGENCY USE ONLY *(Leave blank)*	**2. REPORT DATE** September 2023	**3. REPORT TYPE AND DATES COVERED** Dissertation

4. TITLE AND SUBTITLE INVESTIGATION OF CYCLOTRON RADIATION FROM GRAPHENE-BASED DEVICES	**5. FUNDING NUMBERS**
6. AUTHOR(S) Jordan Planillo	
7. PERFORMING ORGANIZATION NAME(S) AND ADDRESS(ES) Naval Postgraduate School Monterey, CA 93943-5000	**8. PERFORMING ORGANIZATION REPORT NUMBER**
9. SPONSORING / MONITORING AGENCY NAME(S) AND ADDRESS(ES) N/A	**10. SPONSORING / MONITORING AGENCY REPORT NUMBER**

11. SUPPLEMENTARY NOTES The views expressed in this thesis are those of the author and do not reflect the official policy or position of the Department of Defense or the U.S. Government.

12a. DISTRIBUTION / AVAILABILITY STATEMENT Approved for public release. Distribution is unlimited.	**12b. DISTRIBUTION CODE** A

13. ABSTRACT (maximum 200 words)

Current solutions to address the terahertz gap—the range of frequencies from 0.3 THz to 3.0 THz in the electromagnetic spectrum—fall into two broad categories: microwave solutions and photonic solutions. The most promising solutions—high electron mobility transistors and quantum cascade lasers—while capable of producing the desired THz frequencies, are limited from widespread use due to cost and operating environment requirements. Graphene's remarkable material properties have been extensively explored for applications as a replacement for silicon in integrated circuits to novel biological sensors. Of particular interest is graphene's exceptionally high carrier mobility and saturation velocity. These properties make it an excellent candidate for a solid state implementation of a cyclotron radiation source. With the appropriate design, a cyclotron style device that emits THz radiation is possible. This work details the modeling, design, simulation, fabrication, and characterization of graphene-based cyclotrons. Simulated finite element graphene arcs indicate that emissions of 1 THz or greater requires an arc radius of 67 nm or less. Fabricated micron scale models on commercial graphene wafers have demonstrated cyclotron radiation emissions at microwave frequencies (3 GHz–4 GHz), which is independent of the applied stimulus frequencies of 1.73 GHz and 10.16 GHz. Fabrication of nanoscale arc arrays exceeding 1 million per square millimeter was also demonstrated.

14. SUBJECT TERMS terahertz, nanomaterials, graphene, 5G, non-destructive inspection, band-conversion, solid-state cyclotron, nano-cyclotron, infrared, IR, far infrared, FIR	**15. NUMBER OF PAGES** 107
	16. PRICE CODE

17. SECURITY CLASSIFICATION OF REPORT Unclassified	**18. SECURITY CLASSIFICATION OF THIS PAGE** Unclassified	**19. SECURITY CLASSIFICATION OF ABSTRACT** Unclassified	**20. LIMITATION OF ABSTRACT** UU

NSN 7540-01-280-5500

Standard Form 298 (Rev. 2-89)
Prescribed by ANSI Std. 239-18

THIS PAGE INTENTIONALLY LEFT BLANK

Approved for public release. Distribution is unlimited.

INVESTIGATION OF CYCLOTRON RADIATION FROM GRAPHENE-BASED DEVICES

Jordan Planillo
Civilian, Department of the Navy
BS, Rensselaer Polytechnic Institute, 2011
MS, University of Southern California, 2016

Submitted in partial fulfillment of the
requirements for the degree of

DOCTOR OF PHILOSOPHY IN APPLIED PHYSICS

from the

NAVAL POSTGRADUATE SCHOOL
September 2023

Approved by:

Fabio Durante Pereira Alves
Department of Physics
Dissertation Supervisor
Dissertation Chair

Frank A. Narducci
Department of Physics

Jean Paul Santos, NAWCWD

Dragoslav Grbovic
Department of Physics

Todd R. Weatherford
Department of Electrical
and Computer Engineering

Approved by:

Frank A. Narducci
Chair, Department of Physics

Joseph P. Hooper
Vice Provost of Academic Affairs

THIS PAGE INTENTIONALLY LEFT BLANK

ABSTRACT

Current solutions to address the terahertz gap—the range of frequencies from 0.3 THz to 3.0 THz in the electromagnetic spectrum—fall into two broad categories: microwave solutions and photonic solutions. The most promising solutions—high electron mobility transistors and quantum cascade lasers—while capable of producing the desired THz frequencies, are limited from widespread use due to cost and operating environment requirements. Graphene's remarkable material properties have been extensively explored for applications as a replacement for silicon in integrated circuits to novel biological sensors. Of particular interest is graphene's exceptionally high carrier mobility and saturation velocity. These properties make it an excellent candidate for a solid state implementation of a cyclotron radiation source. With the appropriate design, a cyclotron style device that emits THz radiation is possible. This work details the modeling, design, simulation, fabrication, and characterization of graphene-based cyclotrons. Simulated finite element graphene arcs indicate that emissions of 1 THz or greater requires an arc radius of 67 nm or less. Fabricated micron scale models on commercial graphene wafers have demonstrated cyclotron radiation emissions at microwave frequencies (3 GHz–4 GHz), which is independent of the applied stimulus frequencies of 1.73 GHz and 10.16 GHz. Fabrication of nanoscale arc arrays exceeding 1 million per square millimeter was also demonstrated.

THIS PAGE INTENTIONALLY LEFT BLANK

TABLE OF CONTENTS

LIST OF FIGURES

LIST OF TABLES

THIS PAGE INTENTIONALLY LEFT BLANK

LIST OF ACRONYMS AND ABBREVIATIONS

2DEG	Two-dimensional Electron Gas
CNP	Charge Neutrality Point
dBm	Decibel milliWatt
DFG	Difference Frequency Generation
EBL	Electron Beam Lithography
FE(M)	Finite Element (Method)
FEL	Free Electron Laser
GHz	Gigahertz
hBN	Hexagonal Boron Nitride
HEMT	High Electron Mobility Transistor
µm	Micron
nm	Nanometer
nW	nanoWatt
pW	picoWatt
QCL	Quantum Cascade Laser
RF	Radio Frequency
RIE	Reactive Ion Etch
SiO_2	Silicon Dioxide
SNR	Signal to Noise Ratio
SRR	Signal to Reference Ratio
THz	Terahertz
TMIC	Terahertz Monolithic Integrated Circuit
VNA	Vector Network Analyzer

THIS PAGE INTENTIONALLY LEFT BLANK

ACKNOWLEDGMENTS

This work would not have been possible without support from the following organizations and individuals:

Naval Postgraduate School: Drago Grbovic, Pete Crooker, Dave Jenn, James Calusdian, Bob Broadston, Thomas Stapel, Moritz Menge, and Will Guimaraes.

Naval Air Warfare Center Weapons Division—Point Mugu: JP Santos, Max Apalboym, Ricardo Barreto, Ernie Lozano, Nate Quijano, Frank Datello, and Lori Bradley.

Oak Ridge National Laboratory—Center for Nanophase Materials Science: Nick Laverick, Bernadetta Srijanto, Dale Hensley, Kevin Lester, and Daryl Briggs.

THIS PAGE INTENTIONALLY LEFT BLANK

I. INTRODUCTION

The Navy is seeking solutions for secured communications through contested spectrum and for the non-destructive inspection of ship hulls and composite airframes. Cost effective access to the terahertz (THz) range of frequencies is a promising solution to both problems as access to the THz frequency can offer more usable spectra that is resistant to conventional electronic warfare [1]. Additionally, THz radiation can penetrate soft materials which can be used for non-destructive inspection capabilities without the use of ionizing radiation, such as x-rays [2]. Achieving THz radiation in a compact solid-state form has proven difficult due to fundamental limitations in conventional materials and approaches [3]. These limitations may be overcome with a paradigm shift in the form of nanomaterials.

Since its discovery in 2004 [4]–[6] graphene–an atomically thin sheet of covalently bonded carbon atoms–has been touted as a super material known for its excellent mechanical, thermal, and electrical properties. Promising applications range from a new construction material [7] to a room temperature superconductor [8]. While most of the electronics applications for graphene involve its use as a field effect transistor to eventually replace silicon for computing applications, few have explored its use in radio frequency (RF) emissions [9]. Much of graphene's radio frequency (RF) applications have involved design and construction of conventional RF components such as transmission lines [10], waveguides [11], and antennas [12], [13]. More recently, graphene's high carrier mobility [14] and saturation velocity [15] has been explored for its application as a solid state implementation of a free electron laser (FEL) and associated devices such as the wiggler [16], [17] to achieve emissions in THz range of frequencies.

A. TERAHERTZ GENERATION

Located between the infrared spectrum and the microwave spectrum is a range of frequencies spanning from 0.3 THz to 3THz which is largely unused. The terahertz gap exists due to the difficulty in producing radiation at these frequencies [1], [3], [18]. To bridge the gap, one can achieve THz frequencies using microwave-based approaches—

"come up" approaches, or one can achieve THz frequencies with infrared based approaches—"come down" approaches. The most recent "come up" approaches are made possible from advances in switching technologies in the form of high electron mobility transistors (HEMT). The most viable "come down" solutions include difference frequency generation (DFG), photoconductive emitters, and the quantum cascade laser (QCL).

1. Microwave-based Approaches

The terahertz monolithic integrated circuit (TMIC) shows the most promise in bridging the terahertz gap from the RF spectrum. TMIC's utilize Indium Phosphide (InP) based high electron mobility transistors (HEMTs) to achieve these high operating frequencies. InP is the substrate of choice for these applications due to its carrier mobility of μ_n = 5400 $cm^2/V{\cdot}s$ for electrons and μ_h = 200 $cm^2/V{\cdot}s$ for holes [19]. To obtain even higher electron mobilities, InP can be layered with lattice compatible alloys including Indium Aluminum Arsenide (InAlAs) and Indium Gallium Arsenide (InGaAs) which both have electron mobilities as high as $\mu_n = 4{\times}10^4$ $cm^2/V{\cdot}s$ [20], [21]. On their own, these materials exceed electron mobilities of other common semiconductors such as Si (μ_n = 1350 $cm^2/V{\cdot}s$) [22] and Gallium Arsenide (GaAs) (μ_n = 9000 $cm^2/V{\cdot}s$) [23], but when layered onto InP—forming a heterostructure—an even higher electron mobility region is created at the mating surfaces. This interface is called a two-dimensional electron gas (2DEG) [Figure 1]. Electrons in this region have mobilities as high as $\mu_n = 1.5{\times}10^4$ $cm^2/V{\cdot}s$ [24]. InP HEMT based switching technology can operate at speeds up to 1.2 THz at powers as high as 1 mW [25].

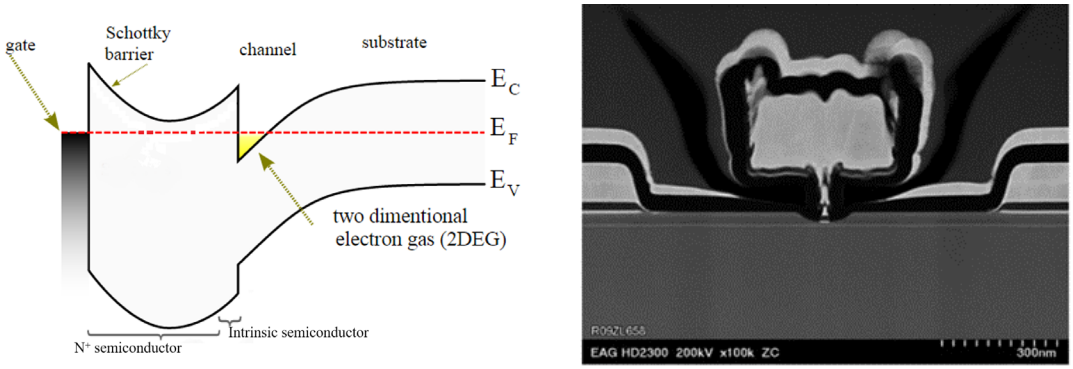

(a) (b)

(a) Band structure diagram of a 2DEG in a heterostructure. Modified under creative commons license [26] (b) InP HEMT cross section with a 30 nm gate width. Source: *Copyright © 2014, IEEE* [25].

Figure 1. 2DEG diagram and InP HEMT

2. Photonics-based Approaches

a. Difference frequency generation (DFG)

To bridge the THz gap from the IR spectrum, the reverse process of frequency multiplication—difference frequency generation (DFG)—can be used. This process is possible by mixing a pump source at frequency ω_p with a signal source at frequency ω_s and obtaining the difference $\omega_{THz} = \omega_p - \omega_s$. DFG is a second order nonlinear optical phenomenon and thus requires high intensities for efficient down conversion from IR to THz for standard materials. Incident power from the pump and signal lasers powers are reasonably high at 1 W each with a resulting THz output power of 0.66 mW. Additionally, for DFG processes that occur in waveguides, the THz output power is also affected by the length of the waveguide—an increase in waveguide length increases the interaction length, thus increasing the output power [27], [28] [Figure 2].

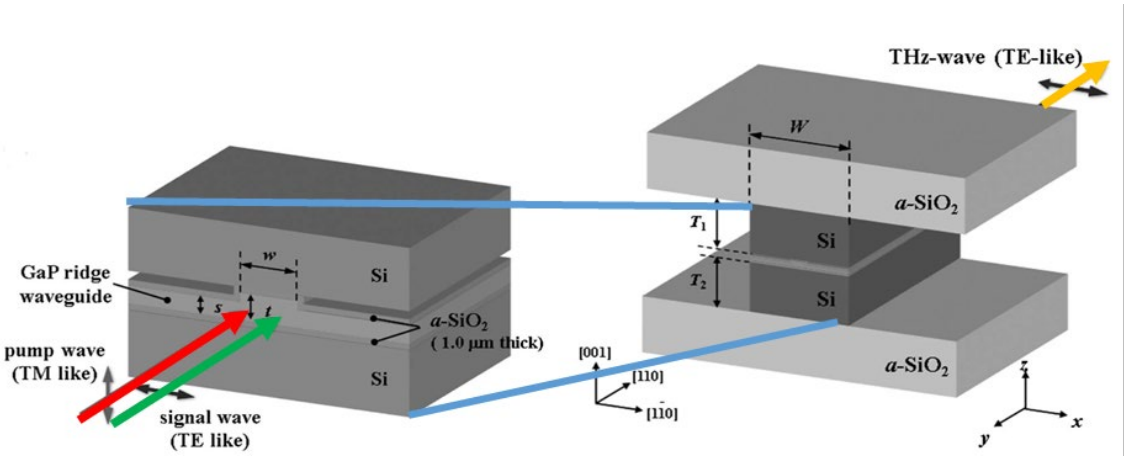

A TM mode pump wave (red) and TE signal wave (greed) are incident on the aperture of the GaP waveguide. As the pump and signal propagate, mixing interactions occur resulting in the output of TE mode THz waves (yellow) in the encapsulating Si layers. Adapted from Saito et al. [26].

Figure 2. DFG in a waveguide

b. Photoconductive Generation

For certain applications, a broadband source for THz radiation is desired compared to the narrowband sources discussed in the previous and future sections. Optically, such a requirement can be met by using photoconductive emitters. THz photoconductive emitter systems consist of a high-speed photoconductor connected to a THz antenna which is driven by an optical pump [Figure 3]. Currently, photoconductive emitters can produce frequencies of 0.1–2 THz and can achieve conversion efficiencies as high as 7.5%. The conversion efficiency of photoconductors is limited by carrier sweep times which can be improved by altering the photoconductive electrode geometry [29].

In order to emit at THz frequencies, sub-picosecond carrier sweep times are necessary. For GaAs substrates, only electrons as far as 100 nm from the surface are swept within a picosecond, which limits the amount of THz output power. A typical electrode structure for a photoconductive emitter consists of an interlaced grating of gold electrodes on the surface of the substrate [30]. The output frequencies of photoconductive emitters are based on the antenna design. A logarithmic spiral antenna was chosen as this geometry supports broadband emission of frequency components. Such a wide band is necessary as the optical pulses result in frequency components ranging from 0.1–2 THz [31].

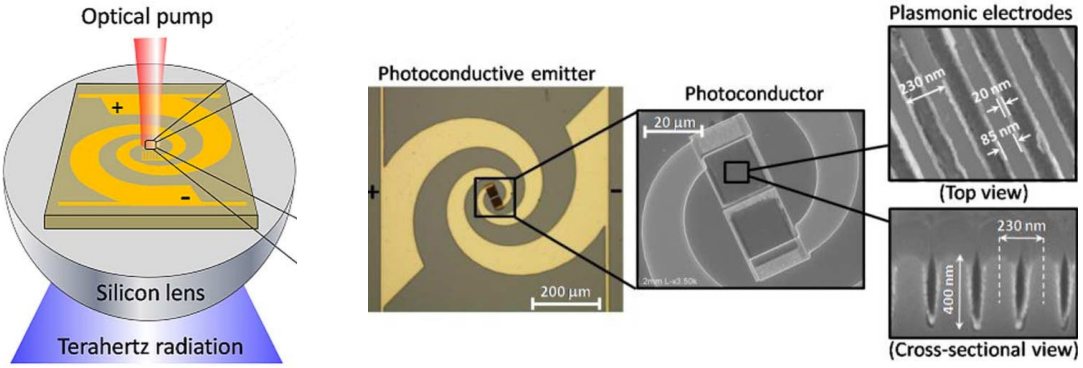

(a) (b)

(a) Photoconductive emitter concept of operation. (b) Photoconductive emitter components from left to right: logarithmic spiral antenna; metallic from antenna to the electrodes; plasmonic electrodes which interface with the semiconductor substrate. Source: *Copyright © 2014, IEEE* [30].

Figure 3. Photoconductive emitter

c. Quantum Cascade Laser (QCL)

For applications requiring narrowband THz emission, the quantum cascade laser offers all of the desired features of a conventional solid-state laser, but at THz frequencies. Unlike conventional solid-state lasers in which the photon energies are near the band gap energy, quantum cascade lasers (QCL) emit photons at several intermediate states between the conduction and valence bands. These states are constructed by compositing several GaAs/Aluminum Galium Arsenide (AlGaAs) heterostructures in series [Figure 4]. The QCL is able to lase at frequencies as low as 4 THz with an output power of 2 mW [32].

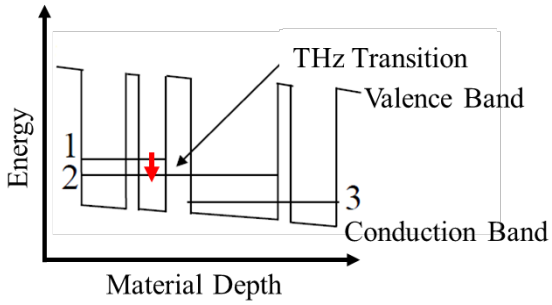

Electrons in the ground state (3) are pumped into an intermediate excited state (1). From state (1) the electrons transition to state (2) via a radiative decay process (red arrow) which results in THz emission. Following the radiative decay process, electrons undergo a non-radiative decay process to return to the ground state. Adapted from Waldmueller et al. [31].

Figure 4. QCL band diagram

While the QCL heterostructures allow for precise control over photon energy, these intermediate stages are highly sensitive to temperature, which can be detrimental to population inversion. To mitigate this, QCLs are either cryocooled or employ optical pumping techniques to populate the highest sub bands [33].

B. CYCLOTRON RADIATION

Electromagnetic radiation, in its most simple case is the radiation from an accelerated point charge, q. The resulting radiated electric field is given by the Lienard–Wiechart potentials [34]:

$$\overline{E} = \frac{q}{c}\left[\frac{\hat{n}\times(\hat{n}\times\dot{\beta})}{R}\right]_{ret} \tag{1}$$

where c is the speed of light, $\hat{n}$ is the unit vector from the source point to the observer, R is the distance from the origin to the observer, and $\dot{\beta}$ is the acceleration normalized by the speed of light with the expression evaluated at the retarded time.

Consider the case of a charged particle in a magnetic field of magnitude, B, with a velocity, v, and mass, m. The charged particle will orbit in a plane whose normal vector coincides with the magnetic field. The orbital velocity, ω, and orbital radius, r, are given by the following relation [35]:

$$\omega = \frac{v}{r} = \frac{qB}{m}. \tag{2}$$

In the case of $R >> r$ and $\beta << 1$, the resulting electric field reduces to that of the rotating electric dipole where the dipole moment is . The cyclotron [Figure 5] is one such device that produces electromagnetic radiation from charges in circular orbit due to a magnetic field.

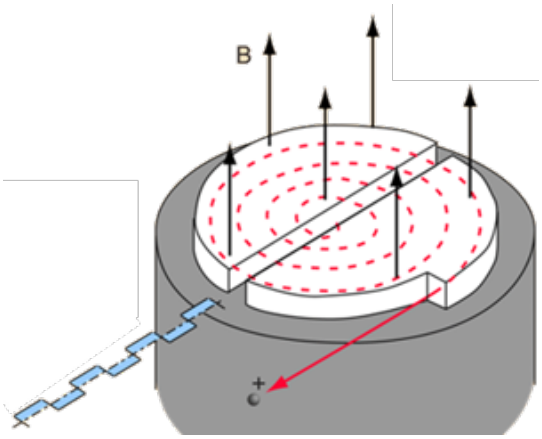

A charged particle at the center of the circular region is subject to initial acceleration by electric field between the "D" shaped components. A magnetic field perpendicular to the plane of the circular region is applied resulting in circular orbits. Adapted from *Hyperphysics* [35].

Figure 5. Cyclotron concept

C. GRAPHENE TERAHERTZ PROPERTIES

Graphene is the name given to the two-dimensional sheet of covalently bonded carbon atoms when it was first isolated by mechanical exfoliation of bulk graphite [5]. The carbon atoms in graphene consist of two offset triangular lattices which forms a hexagonal pattern [Figure 6(a)]. In reciprocal space [Figure 6 (b)], a linear dispersion relation occurs near the intersections of the conduction and valance bands—Dirac points—which results in effective zero mass of the charge carriers in this region [8].

Canonically, the zero effective mass of electrons in graphene was arrived by applying the linear dispersion relation for photons analogy to a pseudo-relativistic case for graphene near the Dirac points [8]:

$$E^2(\vec{k}) = (mc)^2 + \left(\vec{p}(\vec{k}) \cdot c\right)^2, \tag{3}$$

$$\vec{p} = \hbar\vec{k}, \tag{4}$$

where E is the energy [36], $\vec{p}$ is the momentum, and $\vec{k}$ is the wavevector. To arrive at the linear dispersion relation for graphene, the mass term in (3) must be zero and the momentum (4) must only be a function of wavenumber. In graphene, it is said the electrons move with zero effective mass at the Fermi velocity (v_F = 10^8 cm/s), which is analogous to the speed of light, c.

For conventional materials, the effective mass is inversely proportional to the curvature of the dispersion relation [22]. This approach, if applied to graphene, will result in an incorrect conclusion—infinite mass. An alternative, non-relativistic, explanation [37] begins with the treatment of the effective mass of an electron in graphene as a tensor quantity. The effective mass is then redefined as the ratio of momentum to velocity, as opposed to the ratio of force to acceleration. This tensor treatment, along with the linear dispersion relation, has shown than an electron in graphene will have a zero effective mass for impulses applied to parallel to the electron's motion and a non-zero effective mass for impulses applied perpendicular to the electron's motion.

As a consequence of zero effective mass, graphene has exceptionally high carrier mobility of μ_n = 2×10^5 cm^2/V·s [14], [15]. This property of graphene is highly desirable for microelectronics applications and potentially useful for THz emission.

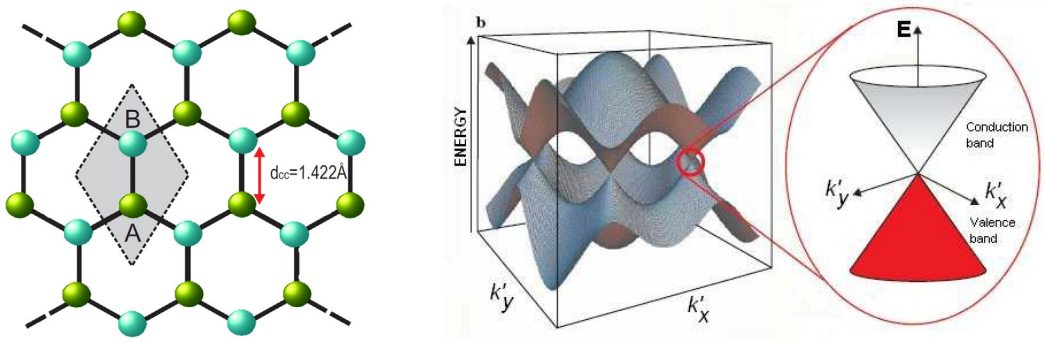

(a) (b)

(a) Real space structure of graphene consisting of two offset triangular lattices resulting in a hexagonal mesh pattern. (b) Reciprocal graphene lattice with linear dispersion relation near the Dirac point. Source: Wojtaszek et al. [36].

Figure 6. Graphene structure in physical and reciprocal space

1. Landau Level Transitions

In the cyclotron explanation given in section IB, the charges orbiting in the magnetic field were assumed to be free particles. In a solid-state medium, electric currents are a continuum of charge flow, not discrete points. If a magnetic field of magnitude, B, is applied to a current bearing device, the charges in the current deflect—the Hall effect [22]. Under high applied magnetic fields (1 T), an electron, e, forms quantized orbits known as Landau levels [38]. In graphene [39], the orbits are defined by the cyclotron frequency ω_c:

$$\omega_c = v_F \sqrt{\frac{2eB}{\hbar}}, \tag{5}$$

where v_F is the Fermi velocity (10^8 cm/s) and $\hbar$ is the reduced Planck constant. The resulting energy levels are given by:

$$E_n = \text{sgn}(n)\sqrt{n\hbar\omega_c}, \tag{6}$$

where sgn(n) is the signum function applied to the Landau index n, which is an integer index corresponding to the energy level. The above relations suggest a particular frequency can be tuned for absorption or emission particularly for THz frequencies [40], [41]. Figure

7 demonstrates a scheme for pumping with a laser, promotion to an excited state, and emission to the ground state.

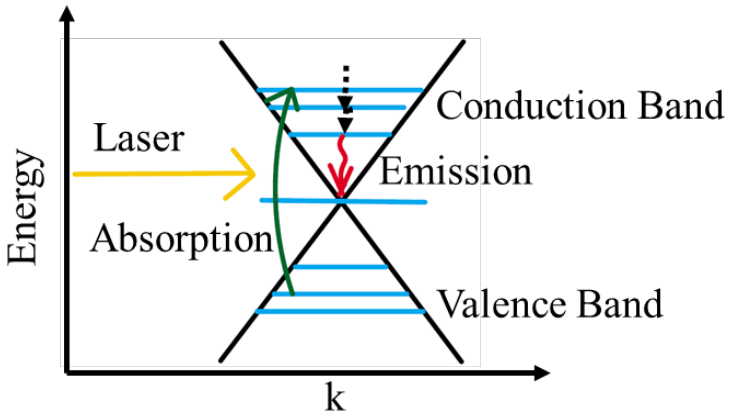

A laser (yellow) pumps a valance electron to an excited state (green). The electron decays via non-radiative processes (black dotted arrows) to an intermediate excited state before finally decaying into the ground state via a radiative process (red). Adapted from Morimoto et al. [38].

Figure 7. Diagram of quantized cyclotron energy transitions

2. Corrugated Graphene

While circular motion is one way of producing tangential acceleration which yields electromagnetic radiation, undulation is another such method while also allowing for a net displacement of the charges [34]. With graphene being a 2D material which conforms to its substrate, it is possible to fabricate a corrugated graphene structure—a wiggler [Figure 8]. Corrugations are defined by their amplitude, A, and period, Λ. For a charge moving with an experimentally achievable fixed velocity, $v = 2\times10^7$ cm/s [42] provided by DC bias, and where corrugation period is much larger than the corrugation amplitude, the emission frequency is given by [16]:

$$f = \frac{v}{\Lambda} \tag{7}$$

and its power is given by a modified Larmor formula [16]:

$$P = \frac{4\pi e^2}{3\epsilon_0 c^3} \frac{A^2 v^4}{\Lambda^4}, \tag{8}$$

where ϵ_0 is the permittivity of free space. One such implementation of a graphene wiggler involves transferring graphene films grown by chemical vapor deposition (CVD) on polymethyl methacrylate (PMMA) on to an etched germanium (Ge) substrate with a device area of 400 μm × 400 μm [17]. Using electron beam lithography (EBL), corrugation periods of 90 nm and 150 nm were patterned. Corrugation amplitudes of 20 nm and 200 nm were achieved with reactive ion etch (RIE). This device is calculated to achieve peak output power at 2.7 THz with an output power to device area figure on the order of 1 nW/cm^2.

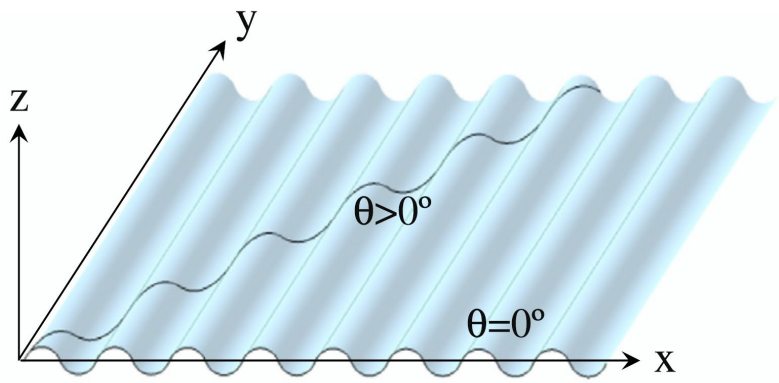

(a)

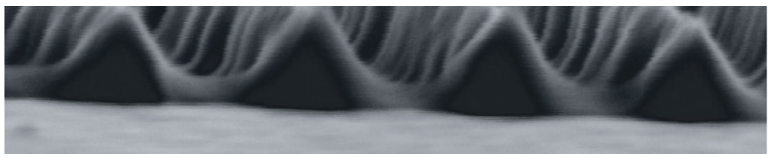

(b)

(a) Trajectories of a charge traversing through sinusoidally corrugated graphene. Source: Tantiwanichapan et al. [16]. (b) SEM cross section of a graphene "wiggler." Graphene on a PMMA film is transferred onto a periodically etched Ge substrate. Corrugation periods of 90 nm 100 nm and amplitudes of 20 nm and 200 nm were fabricated. Adapted from Anwar et al. [17].

Figure 8. Corrugated graphene

3. Curved Planar Graphene

A curved planar graphene sheet geometry is yet another approach that provides tangential acceleration and allows for a net displacement of charges. Rather than using an external magnetic field to provide the centripetal force that accelerates the charges, the graphene is patterned to the desired trajectory to achieve the desired acceleration. This method may be particularly advantageous as the graphene transfer method required for the wiggler method, while reproducible, may not be scalable. While the graphene films grown by CVD occupy a continuous area, monolithic continuous sheets on the order of 1 cm^2 do not currently exist as the graphene grows in grains which range in size from a few microns to tens of microns. Device performance will be hindered due to scattering at the grain boundaries [43]–[45]. Additionally, the corrugations induce localized charge density variations as stresses on the lattice caused by the corrugations locally shift the Fermi level [46]. By explicitly patterning the trajectory, grain boundary can be circumvented if the patterned trajectory is within the size of a grain and can be further improved if a multitude of trajectories are patterned over the graphene film.

4. Latest Developments

As of this writing, there are no further advances in the approaches mentioned in Chapter I, Section C 1 and 2. It is important to highlight that models have been developed and structures have been fabricated. Nevertheless, there has not been a successful experimental demonstration of radiation of any kind yet. These aforementioned approaches mainly focused on parameters and designs specific for THz radiation instead of proving the radiation concept in general at frequencies where instrumentation is mature, such as microwave. Due to the difficulty of generation and detection of THz frequencies, even with known methods, these approaches likely produced a device with no means to verify their hypotheses.

For completeness and awareness, there are other radiation mechanisms for electromagnetic radiation graphene such as Smith-Purcell [47], Cherenkov [48], and plasmonic gratings [49]. These methods are omitted from further discussion in this work as the exact details of the radiation mechanisms diverge from the objective of this work—

cyclotron style radiation. For further information on these methods, consult the list of references.

D. OBJECTIVE AND RESEARCH QUESTIONS

The purpose of this investigation was to study the possibility of cyclotron radiation from curved planar graphene for the case of the semicircular arc as proposed by the author. This investigation began by hypothesizing that graphene is a suitable candidate for a solid-state implementation of a cyclotron radiation source; and when fashioned into semicircular geometries the boundary conditions mimic that of a rotating electric dipole. This hypothesis was first tested with an analytical model, followed by finite element method (FEM) simulations of the electric dipole model and arc geometry designed to operate at microwave and THz frequencies. A suitability study was then performed on commercially obtained graphene wafers to determine if such materials can meet the processing and performance requirements for fabrication of the intended geometries.

The long-term goal is to develop THz emitters by band conversion. THz emitting graphene arcs are on the nanometer scale and require sophisticated fabrication techniques, therefore, as a proof of concept, devices designed for emission in the microwave spectrum were then fabricated with conventional photolithography using the capabilities of the Naval Postgraduate School's microfabrication facilities. These devices were used to provide an experimental demonstration of the cyclotron radiation phenomenon. Lastly, devices designed for emission at THz frequencies were fabricated with electron beam lithography (EBL) using the facilities of the Center for Nanophase Materials at Oak Ridge National Laboratory.

In order to determine the validity and viability of the curved planar graphene approach, the investigation sought to answer the following questions:

- Under ideal conditions, what is the relation of the radius and width of the graphene arcs to output frequency and power? Are there limits to how high or low of a frequency that can be achieved? How do these results affect the design and fabrication of a device?

- Can these geometries be constructed with commercially available graphene? Do they provide the performance needed for the devices? What are the limitations or considerations when using such materials?
- Do these geometries radiate? Is this radiation a characteristic of the cyclotron phenomenon due to the graphene? What is relation between the stimulus frequency and power to the measured emissions?

If successful with a proof of concept at microwave frequencies, then the possibility THz radiation is achievable with the appropriate scaling. Based on the findings of the investigation, efforts to optimize the performance should also be pursued especially in the areas of fabrication to improve device yield; array design to improve net performance; and impedance matching networks optimized for microwave stimulus or for photoconductive operation.

II. MODELING AND SIMULATION

This chapter mostly contains material extracted from the author's publication in *Scientific Reports* [50].

The author proposed a device that lies on a flat substrate plane in which graphene is patterned as a semicircular arc [Figure 9]. Such a device will produce cyclotron radiation by charges traversing along the arc. Such a structure would be highly compatible with existing semiconductor processing techniques, especially in terms of scalability and high density layouts. Structures like this are now feasible since graphene manufacturing processes are mature enough to where whole wafers of single layer graphene (grain size ~10 μm) can be purchased [51]. To model such a device and obtain performance estimates, the first assumption is that all the available charge carriers in the semicircular arc are concentrated in a singular point charge traversing along the arc's inner radius (r_{arc}). Next, the singular point charge moves at graphene's room temperature saturation velocity (v_{sat})of 4.25×10^{7} cm/s [15]. For a sufficiently large and suddenly applied field, the charge carriers in the graphene will accumulate in a manner resembling a point charge [52], [53], at the inner radius of the arc.

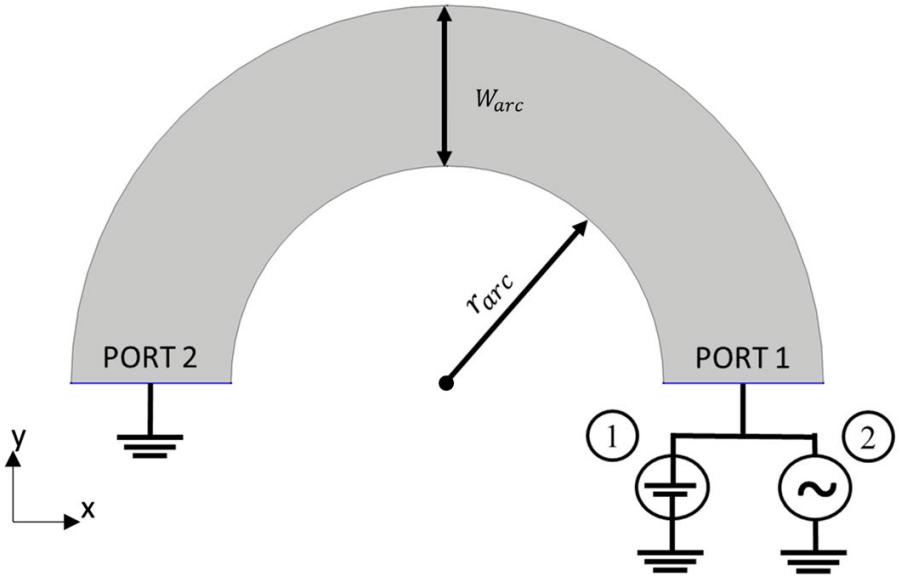

In the dipole model, all of the arc's charges are concentrated at a single point and traverse a semicircular trajectory at a radius r_{arc}. The motion of the charges is expected to produce cyclotron radiation at frequencies inversely proportional to r_{arc}. For the finite element DC simulation (1), a constant 1V was applied. For the finite element RF simulation (2), signals at 4 GHz, 10 GHz, and 40 GHz of 1V amplitude were applied to port 1.

Figure 9. Schematic diagram of the graphene arcs

While graphene's saturation velocity offers superior speed compared to most semiconducting materials, this velocity is still nowhere close to the relativistic speeds of electros found in free electron lasers, wigglers, or synchrotron light sources [54]. This implementation of a solid-state cyclotron radiation source operates in the non-relativistic regime and thus can be initially modeled as a rotating dipole [55]. When reduced to this classic problem, this device is expected to emit radiation at a frequency equivalent to its angular velocity at a power given by the Larmor formula:

$$P = \frac{q^2 a^2}{6\pi \grave{o}_0 c^3}, \tag{9}$$

where q is the effective single point charge of the graphene arc—the product of the carrier density of graphene and the arc area, a is the charge's centripetal acceleration ($a = v_{sat}^2/r_{arc}$), ϵ_0 is the vacuum permittivity, and c is the speed of light in vacuum.

For fixed particle velocity v_{sat} and target frequency f, the required arc radius is $r_{arc} = v_{sat}/2\pi f$. The relation of r_{arc} to frequency is displayed in Figure 10. For microwave frequency operation, a design radius and arc width of 10 µm was chosen as this was close to the smallest radius that could be produced with in-house photolithography capabilities. The corresponding frequency is 6.7 GHz. For target frequencies 0.5 THz and 1.0 THz, the radii are 135 nm and 67 nm respectively. For both of these target frequencies, an arc width of 100 nm was chosen as it is sufficiently wide to avoid quantized current behaviors in the graphene nanoribbon regime [56], [57]. These parameters can be easily manufactured with existing semiconductor processing methods while also being within the constraints of the current state of the art of graphene manufacturing. For ideal operation, such a device must fit within a grain of graphene, nominally 10 µm x 10 µm. To ensure that the assumption of uniform circular motion is valid, arc lengths must be less than graphene's mean free path, nominally ~1-2 µm at 293 K at carrier concentrations of 10^{12} cm^{-2} [14], [58].

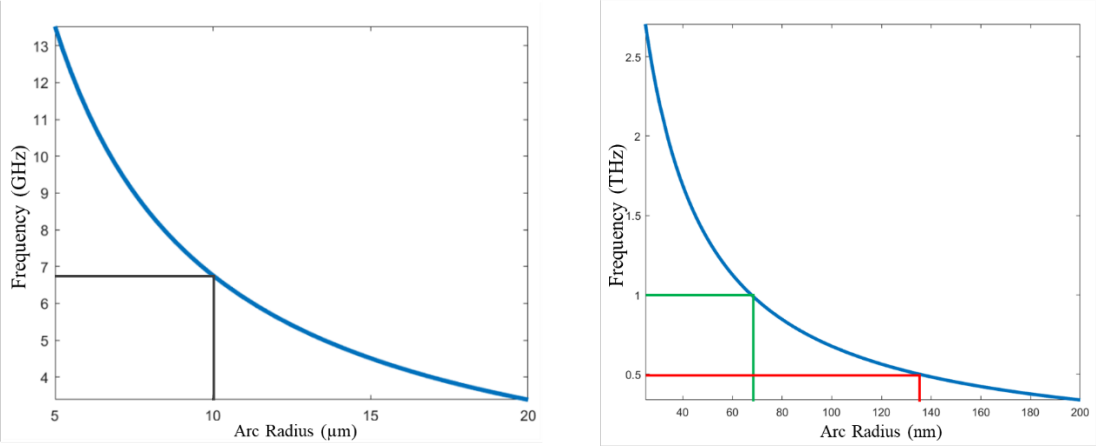

(a) (b)

The target frequencies given by $f = v_{sat}/2\pi r_{arc}$ (a) 6.7 GHz (b) 0.5 THz and 1.0 THz require an arc radius of 10 µm, 135 nm and 67 nm respectively for a rotating dipole with a tangential velocity of $v_{sat} = 4.25\times10^7$ cm/s.

Figure 10. Trendline of emitted frequency vs. arc radius

A. ANALYTIC ROTATING DIPOLE MODEL

For a rotating dipole, the solutions to Maxwell's equations yields the following radiated fields in spherical coordinates [55]:

$$\vec{E} = \frac{\mu_0 p_0 \omega}{4\pi r}\Big\{\cos(\theta)[\cos(\omega(t-\tfrac{r}{c}))\cos(\phi)+\sin(\omega(t-\tfrac{r}{c}))\sin(\phi)]\hat{\theta} \\ -[\cos(\omega(t-\tfrac{r}{c}))\sin(\phi)+\sin(\omega(t-\tfrac{r}{c}))\cos(\phi)]\hat{\phi}\Big\} \tag{10}$$

$$B = \frac{\mu_0 p_0 \omega}{4\pi rc}\Big\{\Big[\cos(\omega(t-\tfrac{r}{c}))\sin(\phi)+\sin(\omega(t-\tfrac{r}{c}))\cos(\phi)\Big]\hat{\theta} \\ +\cos(\theta)\Big[\cos(\omega(t-\tfrac{r}{c}))\cos(\phi)+\sin(\omega(t-\tfrac{r}{c}))\sin(\phi)\Big]\hat{\phi}\Big\} \tag{11}$$

where p_0 is the dipole moment magnitude, ($p_0 = q \cdot r_{arc}$), ω is the charge's angular velocity ($\omega = v_{sat}/r_{arc}$), μ_0 is the vacuum permeability, t is the time parameter; r, θ, and ϕ are the respective radial, altitude, and azimuth coordinates with corresponding unit vectors $\hat{r}$, $\hat{\theta}$, and $\hat{\phi}$.

The concept of operation requires all the available charges in the graphene arc to be concentrated into a single point charge. Such a condition can at best be guaranteed for a time less than or equal to the mean scattering time in the substrate. Consequently, the arc length of the graphene arc should be less than the mean free path. For longer lengths, scattering mechanisms will adversely affect the uniform circular motion required in rotating dipole model. Furthermore, in a solid-state implementation, the uniform circular motion can only hold while charge carriers are in transit and not being injected or recombined at the source and drain terminals. Lastly, the rotating dipole model has to be modified to accommodate the semicircular trajectory of the carriers—unlike the circular motion of the classical problem.

Having constrained the design to a semicircular arc, the transit time of the charge carriers is valid only for one half of an orbital period in the classic rotating dipole problem. To understand the behavior of this now modified problem, equations (10) and (11) are multiplied by a window function [*H(t) – H(t – T/2)*], where *H(t)* is the Heaviside step

function [59]. A Fourier transform of the modified classical solution is calculated over the valid times of 0 to $T/2$ where T is the orbital period in the classic problem. It is anticipated that this modified problem will not radiate at a single frequency like the classic problem in which a Fourier transform of the temporal solution yields a Dirac delta function in frequency space centered at the angular velocity. Instead, a spreading of the frequencies is expected to be centered about the angular velocity of the rotating dipole. If that is the case, then the shape of the spectrum would need to be determined in addition to the frequency that yields the most power. A dimensionless and reparametrized expression for the Fourier transformed fields is given in equation (12) where the dimensionless frequency, x, is the ratio of the frequency parameter ω to the charge's angular velocity ω_0 ($\omega_0 = v_{sat}/r_{arc}$). Given the equivalence of the electric and magnetic fields by multiplication of an orthogonal unit vector and a factor of the speed of light, depending on the unit system— only the electric field is shown:

$$\vec{E}(x,\phi,\theta) = \frac{(1+e^{-i\pi x})(\cos\phi - ix\sin\phi)\hat{\phi} + \cos\theta(1+e^{-i\pi x})(\cos\phi + ix\sin\phi)\hat{\theta}}{x^2-1}. \qquad (12)$$

An expression for dimensionless Fourier transformed Poynting vector $\vec{S} = \vec{E} \times \vec{H}$ can be written as follows:

$$\vec{S} = \frac{2(1+\cos(\pi x))[x^2(1-\cos^2\phi\sin^2\theta)+1-\sin^2\phi\sin^2\theta]}{(x^2-1)^2}\hat{r}. \qquad (13)$$

From the dimensionless Poynting vector, critical values for this expression are sought to understand how the power output S is related to the dimensionless frequency x. A numerical evaluation of the Poynting vector expression yields a maximum at $x \approx 1.36$ [Figure 11]. The resulting pattern radiates in all directions, but is more biased along the x-axis [Figure 12]. For $x = 1$, the expression for the dimensionless Poynting vector yields the same value everywhere in the horizontal plane—a result identical to the unmodified problem. Lastly, for frequencies ranging from $0 < x < 1$ the classic dipole shape is recovered in which the lobes are oriented along the x-axis and no radiation along the y-axis. Another

maximum is observed at $x \approx 3.6$, however there will not be a large contribution at this frequency or any other frequencies beyond the first peak at $x \approx 1.36$.

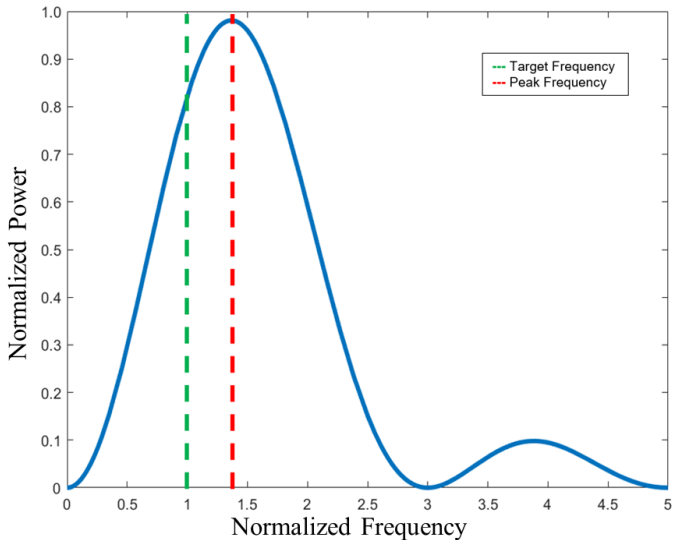

The designed target frequency (green) is recovered in the transient dipole model. In addition there is a peak emission that occurs at a normalized frequency at ~1.36 (red). A secondary peak occurs at ~3.6. The width between the first two nodes of this distribution is 3 times the target frequency. The width between the 2nd and 3rd nodes is 2 times the target frequency.

Figure 11. Calculated frequency spectrum for transient rotating dipole lasting ½ of a full orbital period

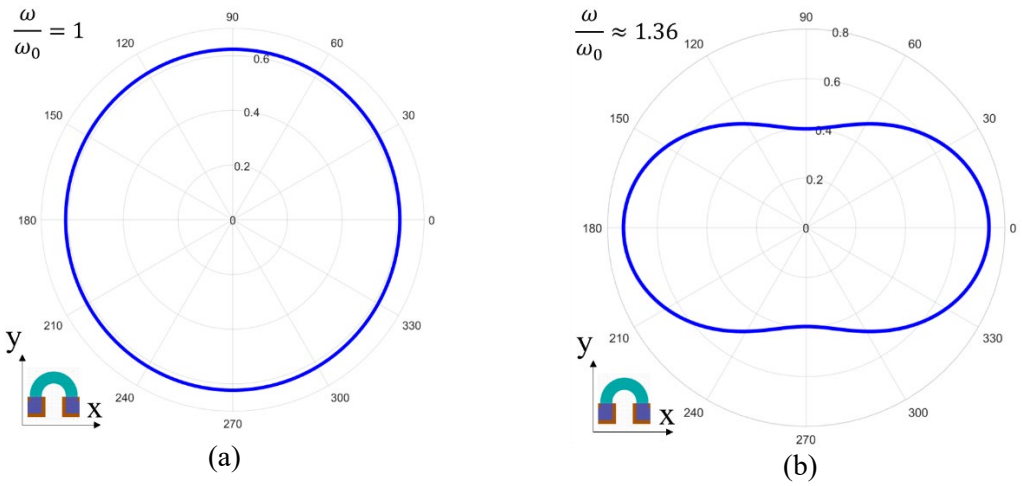

(a) Radiation pattern for normalized frequency equal to 1. The circular pattern is identical to the steady state rotating dipole in which the emitted frequency and angular velocity are equivalent. Power is distributed uniformly in the plane of rotation at this frequency. (b) Radiation pattern for normalized frequency equal to ~1.36. Power is distributed in all directions of the orbital plane but is more biased along the x-axis.

Figure 12. Calculated radiation patterns for transient rotating dipole lasting ½ of a full orbital period in the orbital plane

B. SIMULATION METHODS

Having produced an analytical model, finite element simulations of the simple dipole model in both steady state and transient conditions followed by a semicircular arc of graphene in steady state and transient conditions were performed. In COMSOL Multiphysics, a point dipole of the was created with charge equivalent to the sum of all free carriers of the graphene arcs that correspond to each target frequency (6.7 GHz, 0.5 THz and 1 THz). This value is obtained by multiplying the arc area by the charge density. In this study, charge density of 10^{12} cm^{-2} was used as this value represents room temperature graphene with mean free paths on the order of 1 μm [14].

For the 6.7 GHz system the effective point charge corresponds to 9.46 million electrons. For the 0.5 THz system, the effective point charge corresponds to 1164 electrons while the effective point charge for the 1 THz system corresponds to 739 electrons. Using the RF module in COMSOL (Electromagnetic Waves: Frequency Domain solver), the

charge starts at a position $\vec{r}(r,\phi,\theta) = (r_{arc}, 0, \pi/2)$ and orbits the origin in a counterclockwise manner at the saturation velocity. In the steady state condition, the charge is allowed to make complete orbits like in the classic rotating dipole problem. A scattering boundary condition was defined for a sphere whose radius is 10 times the corresponding arc radius ($r_{boundary}$ = 10 r_{arc}). This model was used to calculate the maximum power output and is compared to the Larmor power formulations.

In addition, a transient dipole model (Electromagnetic Waves: Transient Solver) was developed to capture the frequency spectrum and radiation pattern. Much like the steady state model, all the arc's charge is concentrated to a point and orbits the origin in a counterclockwise fashion at a fixed radius. Unlike the steady state model, the transient model is only valid for ½ of an orbital period. The system is expected to emit a range of frequencies in which the target frequency is emitted uniformly in the plane of rotation.

More realistic models were developed to help prove the concept, where a finite arc width (100 nm for 0.5 THz and 1 THz; 10 μm for 6.7 GHz) were considered. The graphene layer was modeled as a boundary with sheet resistivity specified by the manufacturer 430 Ω/sq [51]. First, using COMSOL's AC/DC module, a direct current (DC) simulation was performed. The straight edges of the arc were set as ports with fixed potential where one was ground and the other 1V. This simulation allows for verification of the field gradient and current flow along the arc. Next, a steady state simulation (Electromagnetic Waves: Frequency Domain Solver) of the arcs stimulated at their respective target frequencies was performed to calculate the maximum power output. Lastly, a transient simulation (Electromagnetic Waves: Transient Solver) was performed on the arcs for a time of ½ of a full orbital period with a Gaussian pulse stimulus centered at 40 GHz, 10 GHz, and 4 GHz. These stimulus frequencies were chosen as they can be readily obtained with existing technology. For more information about the simulations, see supplemental section.

C. FINITE ELEMENT ROTATING DIPOLE MODEL

The simulations for the dipole model agree with the analytical model in that the target frequency is achieved. However, the peak power emission is at a frequency greater than the target frequency. For the 6.7 GHz system, the peak power occurs at 8.64 GHz. For

the 0.5 THz system, the peak power occurs at 0.67 THz. For the 1 THz system, the peak power occurs at 1.17 THz [Figure 13]. Like the analytical studies, additional peaks for the THz systems at about 3 times the target frequency are present. The simulations for the 6.7 GHz design only produced the first peak as the solver would not converge for frequencies beyond this.

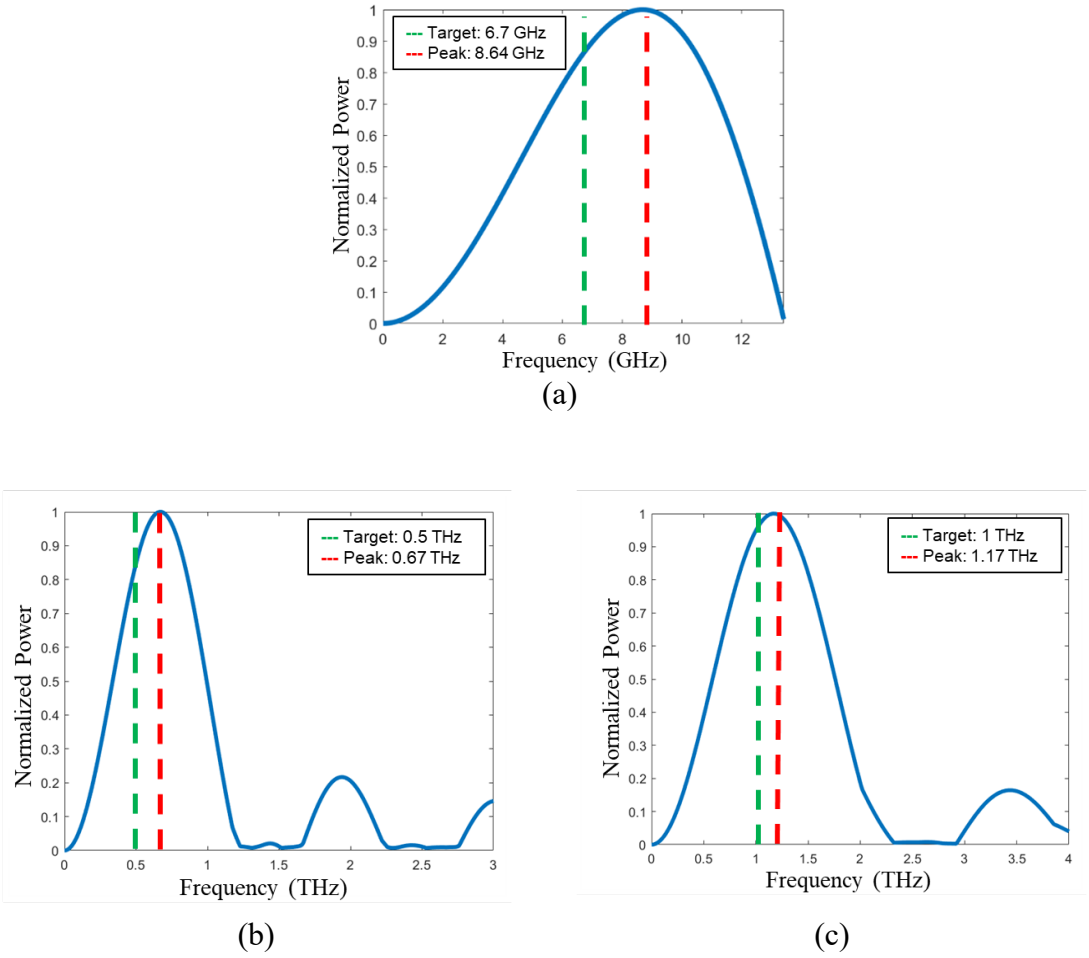

(a) Frequency spectrum of a simulated 6.7 GHz system. A peak is observed at 8.64 GHz. (b) Frequency spectrum of the simulated 0.5 THz system. A peak emission is observed at 0.67 THz. (c) Frequency spectrum of the simulated 1 THz system. A peak emission is observed at 1.17 THz

Figure 13. Simulated frequency spectra for the transient rotating dipole model

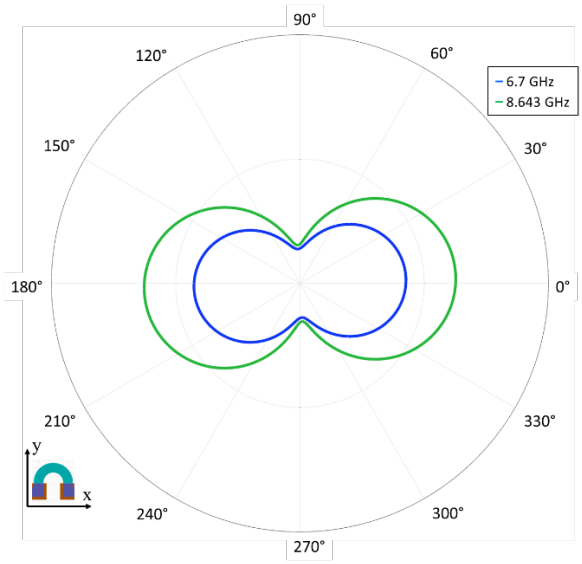

(a)

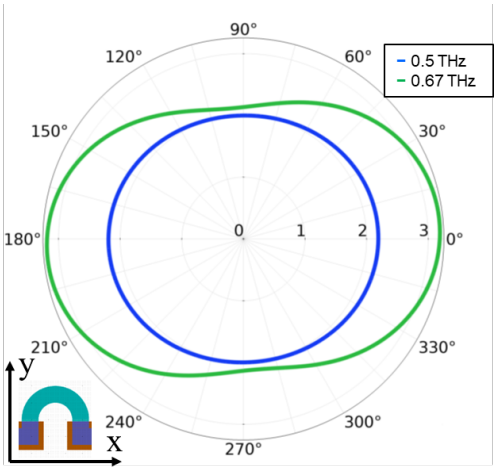

(b)

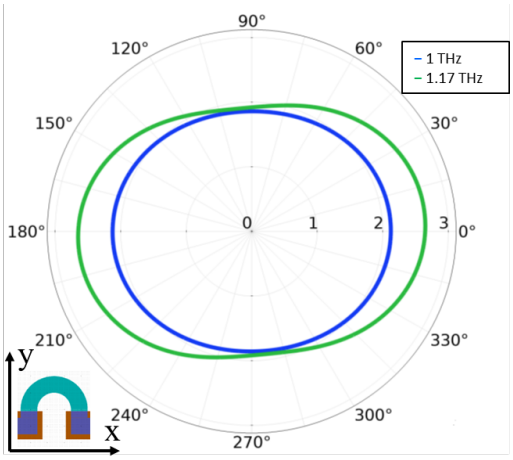

(c)

(a) Radiation pattern for the 6.7 GHz system. The target and peak frequencies both radiate in all directions, but heavily biased toward a linear dipole oriented along the y-axis. (b) Radiation pattern for the 0.5 THz system. The design frequency of 0.5 THz (blue) radiates uniformly in all directions in the plane of rotation. The peak frequency 0.67 THz (green) radiates in all directions in the orbital plane, but is more biased along the x-axis. (c) Radiation pattern for the 1 THz system. The design frequency of 1 THz (blue) radiates uniformly in all directions in the plane of rotation. The peak frequency of 1.17 THz radiates in all directions of the orbital plane, but is biased along the x-axis.

Figure 14. Simulated radiation patterns for the transient rotating dipole model in the orbital plane

In terms of spatial distribution, the target frequency emits uniformly in the plane of rotation in agreement with the theoretical calculations [Figure 14] for the THz designs. While the microwave designed system encapsulates the predicted frequencies, the radiation patterns for both target and peak frequencies radiate in all directions in the plane of rotation, but not as uniformly as predicted by theory. The pattern is more like a linear dipole oriented along the y-axis. From the steady state dipole simulations, the 6.7 GHz system emits a total power of 184.4 nW, the 0.5 THz system emits a total power of 15.55 pW and the 1 THz system emits a total power of 25.4 pW. The simulated steady state dipole power emissions for all cases slightly overestimate the analytical results of 164.3 nW for the 6.7 GHz system, 13.8 pW for the 0.5 THz system, and 22.24 pW for the 1 THz system.

D. FINITE ELEMENT ARC MODEL

The arc simulations were performed to determine the effect of finite device width. For all designs, the target frequencies of 6.7 GHz, 0.5 THz and 1 THz are achieved [Figure 15]. For the 6.7 GHz design, the peak power is emitted at 9.045 GHz. For the 0.5 THz design, the peak power is emitted at 0.57 THz, while the 1 THz design's peak power is emitted at 1.33 THz. Total power is calculated to be 414.6 nW for the 6.7 GHz arc,18.4 pW for the 0.5 THz arc and 13.8 pW for the 1 THz arc. Due to limitations in COMSOL's capabilities, the radiation patterns for the arcs did not capture the particle dynamics of the charge carriers in the arc [Figure 16]. As a result, the expected radiation pattern from a rotating charge is not produced by the simulations. The shape instead resembles that of a dipole oscillating along the x-axis.

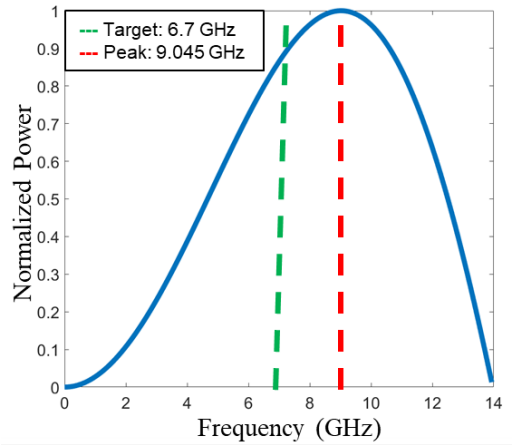

(a)

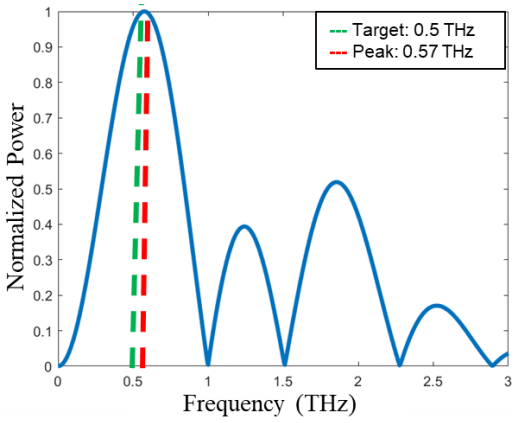

(b)

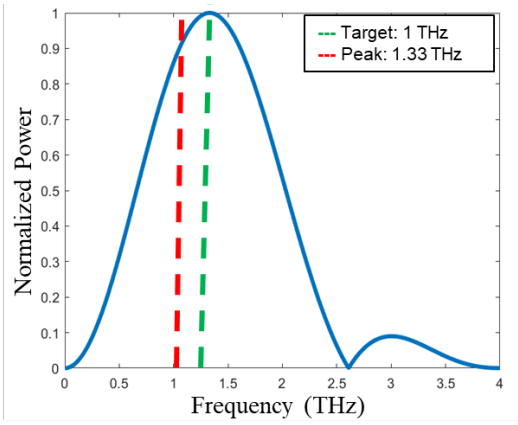

(c)

(a) Frequency spectrum of the 6.7 GHz system. A peak occurs at 9.045 GHz (b) Frequency spectrum of the 0.5 THz system. A peak occurs at 0.57 THz with secondary peak occurring at 1.8 THz. A tertiary peak occurs at 1.25 THz, previously not predicted by the dipole model. (c) Frequency spectrum of the 1 THZ system. A peak occurs at 1.33 THz with a secondary peak at 3 THz.

Figure 15. Simulated frequency spectra for the transient arc

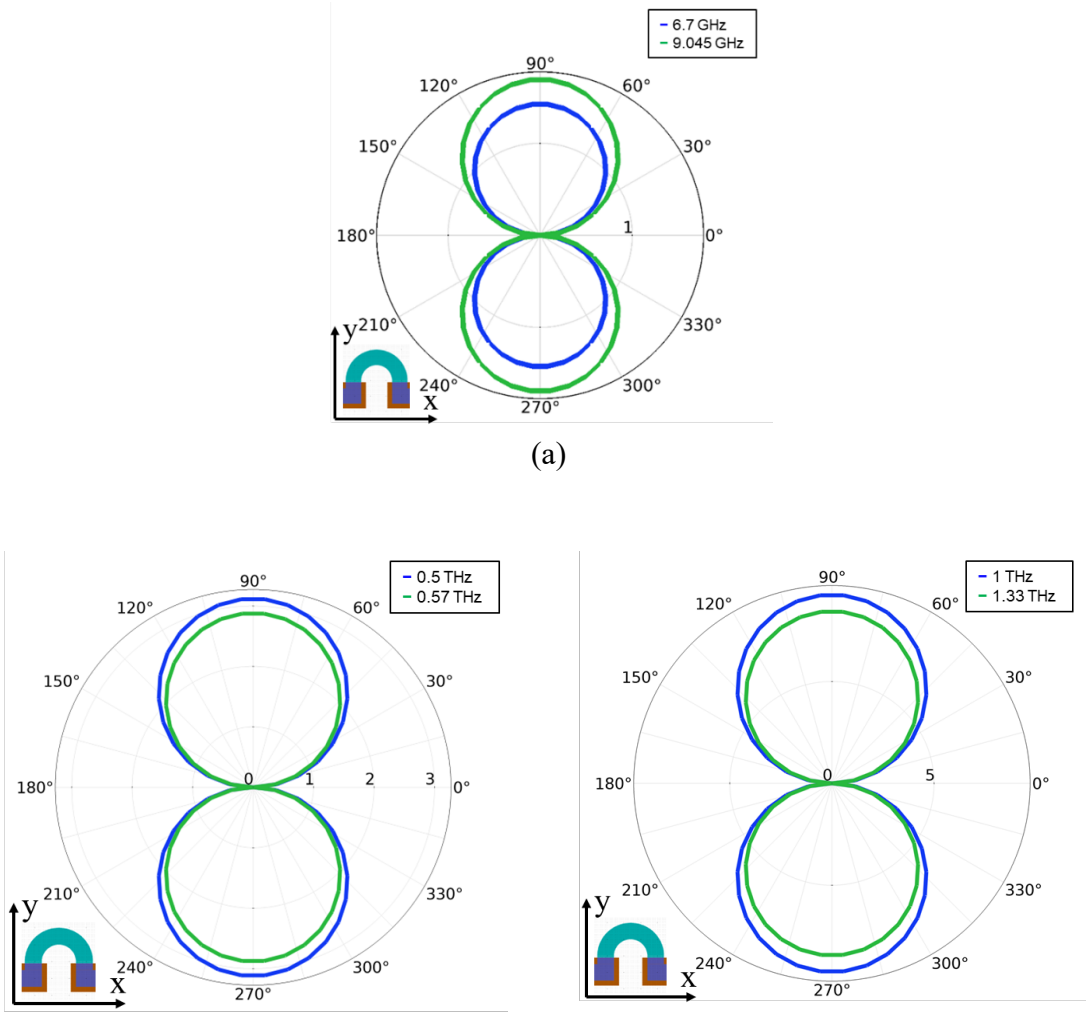

(a) The 6.7 GHz system (b) The 0.5 THz system and the 1 THz system (c) at the design frequency (blue) and at peak emission (green). The finite element software used does not account for particle dynamics and hence does not produce the expected circular rotating dipole radiation pattern. The shape instead resembles a dipole oscillating along the x-axis.

Figure 16. Simulated radiation patterns for the transient arc models in the orbital plane

To illustrate the deviation from the point charge models, DC simulations were performed on the respective arcs [Figure 17]. The simulations with an applied bias of 1V indicate that current flows from the source, on the right hand side, to the drain, on the left, along the field gradient. The current is most closely concentrated towards the inner radius

as indicated by arrow length and thickness. Unlike the point charge assumption, in the arc, charges are distributed along the width of the device.

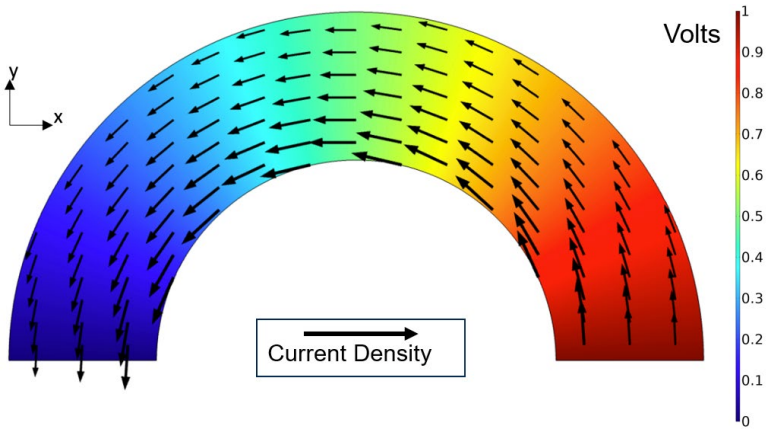

Current flows along the arc with the highest current density at the inner radius as indicated by arrow size. This is unlike the point charge assumption in which all of the charge located at the inner radius.

Figure 17. Simulated current density under DC bias of 1V potential difference between source and drain

Another deviation from the point charge model pertains to device stimulation. For the concept of operation, a transient pulse with a voltage amplitude of 1V is applied between source and drain terminals. A 40 GHz Gaussian pulse was used in the preceding simulations as it is a sufficiently high frequency that is still attainable with existing technology. With lower frequency stimuli, the frequency spectrum is expected to be degraded with more spurious components being present. The emission spectrum was obtained for additional stimuli at 4 GHz and 10 GHz. Figure 18 shows the spectral response of the 0.5 THz system. Remarkably, the spectrum shape is consistent over all the stimulus frequencies. The simulation results over a set of different stimulus frequencies [Figure 18] indicate that the emission spectrum is independent of the stimulus frequency. This result was not expected as it is anticipated that the device would be less responsive at frequencies farther away from the target frequency and thus the emission spectrum would more likely consist of spurious emissions. The device's emission spectrum is a function of its geometry defined by the arc's inner radius.

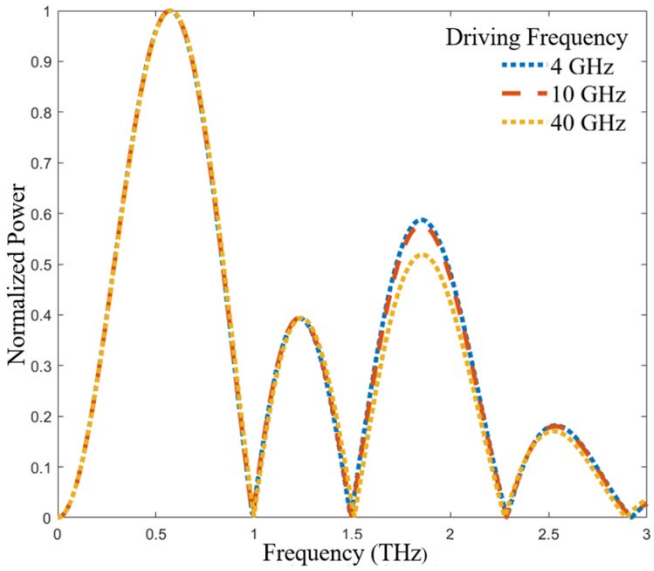

Normalized spectra over the set of applied stimuli for the 0.5 THz design. For all stimuli, the shape is consistent. The 4 GHz and 10 GHz slightly overshoot the 40 GHz secondary peak at 1.8 THz.

Figure 18. Effect of stimulus frequency on emission spectrum with 4 GHz, 10 GHz, and 40 GHz stimuli

E. ANALYSIS

In this chapter, the possibility of terahertz emission from a solid-state cyclotron-radiation emitter device with a graphene substrate has been demonstrated. A simplified analytical model showed that the device can first be modeled as the classic rotating dipole problem by assuming that all the substrate charges can be treated as a single point charge. Two finite element models were also created to first, verify the analytical results and second, account for the finite dimensions of the graphene arcs. Both output power and spectral characteristics were obtained by all three models. Table 1 shows the calculated output powers. For the 6.7 GHz system, all calculations agree to the same order of magnitude; however, the arc model overestimates the output power of the other models by over a factor of 2. On average, powers of 254 nW ± 55% can be expected for this design. For the 0.5 THz system all calculations agree within the same order of magnitude and are within 15% of the mean—15.9 pW. For the 1 THz system, the simulated dipole agrees with

the Larmor calculation while the simulated arc underestimates the output power by nearly 10 pW. On average, the 1 THz design should emit 20.5 pW ± 29%.

Table 1. Calculated output power of the graphene cyclotrons

Model	**Power (nW)**	**Power (pW)**	
	6.7 GHz	**0.5 THz**	**1 THz**
Analytical	164	13.8	22.0
FE Dipole	184	15.5	25.4
FE Arc	415	18.4	13.8
Average	254 ± 55%	15.9 ± 55%	20.5 ± 29%

In terms of radiated frequency spectrum, the transient operating nature of this device implies that even with the point charge assumption that is constrained to orbit a fixed radius, the emission spectrum would result in a distribution of frequencies. This distribution is expected to contain a frequency equivalent to the angular velocity of the orbiting charge with a peak power emission at a frequency ~1.36 times the angular velocity. For the 6.7 GHz system, the simulated dipole and simulated arc models produce the target frequency as well as peaks occurring at 8.64 GHz and 9.045 GHz, respectively.

For the 0.5 THz system both the simulated dipole and the simulated arc produce the target frequency of 0.5 THz and their peak emissions occur at 0.67 THz and 0.57 THz respectively. This gives a frequency ratio of 1.34 for the simulated dipole and 1.14 for the simulated arc. For the 0.5 THz system, the simulated dipole approaches that of the analytically predicted peak while the simulated arc falls slightly short of the analytical result. The 1 THz system, however, yields a ratio of 1.17 for the simulated dipole and 1.33 for the simulated arc. For all systems, each of their respective simulations slightly underestimate the predicted peak frequency. The ratios for each design is summarized in Table 2. It was expected that the simulated dipoles would yield the closest values since these approximations are equivalent to the analytical calculations. Given these results, one can expect the peak frequency to be higher than the target frequency by a factor 1.14 and 1.36 times the angular velocity.

Table 2. Peak frequency to target frequency ratios

Model	Target Frequency		
	6.7 GHz	**0.5 THz**	**1 THz**
Analytical peak to target ratio	1.36	1.36	1.36
FE Dipole peak to target ratio	1.29	1.34	1.17
FE Arc peak to target ratio	1.35	1.14	1.33

With the aforementioned results, one can design a system in which the desired frequency is the peak frequency and not the orbital angular frequency. Such a system could then achieve the same frequency emission with a larger physical footprint than a system in which the angular velocity is the target frequency. This would be advantageous from a prototyping fabrication perspective as the larger footprint would provide additional margin for the processing steps possibly yielding higher fidelity patterns over a design with smaller margins. It is important to mention that, designing for the peak emission will come at the expense of the uniform radiation pattern [Figure 12]. The simulated device configuration shows that the excitation frequency has no effect on the resulting cyclotron radiation emissions. This result suggests that such a device can be used as a band converter, but further investigation is required.

The predicted device power per area is on the order of 1 nW/cm^2. This device performance is in the upper range of existing work on graphene wigglers which are expected to emit 1 pW/cm^2 to 10 nW/cm^2 [17]. Such power can be realized with large scale repetition using existing semiconductor processing methods. Given the geometric constraints of a semicircle, it is possible that the desired radiation pattern can be preserved over an array of these devices by having alternating oriented semicircles such that the source and drain terminals also alternate instead of a simple repetition and translation of the semicircle and associated interconnects. Such an implementation would piecewise form a full circle and would save on manufacturing space by reusing a terminal that can be used by two neighboring units. The results of these simulations are promising enough to fabricate the proposed device and seek experimental verification.

THIS PAGE INTENTIONALLY LEFT BLANK

III. GRAPHENE CHARACTERIZATION

This chapter mostly contains material extracted from the author's publication in MDPI *Electronics* [60].

Having shown that electromagnetic emissions from a semicircular arc of graphene is possible based on theory and simulation, the next step towards implementation is to characterize micron scale devices on commercially available graphene wafers. Of particular interest is to determine graphene quality, patterning fidelity, carrier density, and carrier mobility. This dissertation will focus exclusively on the characterization of graphene from chemical vapor deposition (CVD). Graphene derived from CVD is a promising source for graphene electronics due to its scalability where areas as large as common standard wafer sizes (4," 8," 12") and larger cand be manufactured. Current CVD graphene methods also allow for graphene to be transferred to any substrate [43]–[45], [61], [62] allowing for non-conventional electronics applications. The scalability of CVD graphene inherently has a cost advantage compared to exfoliated graphene and the technology is mature enough where CVD graphene wafers can be readily purchased [51]. Given the incredibly low output power of an individual graphene arc (pW to nW) CVD graphene, combined with the repeatability of semiconductor processing methods, this method should be suitable for arrays of graphene arcs on the order of hundreds of thousands to millions for use as a practical source of electromagnetic radiation.

Early research in graphene, both exfoliated and CVD derived, was conducted on silicon dioxide (SiO_2) insulator on Si wafers as the de facto standard, due to the ubiquity and maturity of these materials. Such research has shown that SiO_2 greatly reduces graphene's carrier mobility and limits it by on order of magnitude to 4×10^4 $cm^2/V\cdot s$ [58]. The inclusion of hexagonal Boron Nitride (hBN) as a lattice compatible insulator with graphene yields much higher mobilities [63]–[66]. Just as in the early research in graphene, hBN was obtained from exfoliation of BN crystals. Methods for CVD derived for hBN have been developed that, like CVD graphene, are transferrable to any substrate [67], [68]. The technology for CVD hBN is mature enough where hBN wafers and graphene on hBN wafers can be purchased commercially [51].

Quality and suitability assessment of the CVD graphene entails the fabrication, characterization, and measurement of identical Hall bar geometries of graphene on both SiO_2/Si and hBN/ SiO_2/Si substrates on the 4" wafer standard patterned with conventional photolithography. Previous research has shown the utility of large scale graphene in electro-optic devices due to its thin and nearly transparent nature [62], [69], [70]. CVD graphene processed with conventional photolithography can be a cost-effective approach towards the realization of graphene electronics and the possibility of monolithic graphene integrated circuits and to compare the electrical properties of otherwise identical graphene devices on SiO_2 and hBN, respectively.

A. METHODS

To demonstrate the process compatibility of the CVD graphene wafers with the fabrication capabilities at NPS, an assortment of rectangular and semicircular geometries with sizes ranging from 5 µm × 50 µm to 100 µm × 1000 µm were designed by the author as shown in Figure 19. Successful processing of the smallest devices would demonstrate the pattern transfer resolution from the mask to the substrate. Successful processing of the largest devices would test the limits of electrical continuity at the millimeter scale. Semicircular device geometries were also chosen to demonstrate patterning fidelity as curved geometries may process differently than rectangular geometries. Lastly, device arrays were designed to test process repeatability and device yield over a 1 cm^2 area. The most extensive testing was performed on the large 100 µm × 1000 µm devices on both SiO_2/Si and hBN/ SiO_2/Si substrates in which electric field response and Hall effect measurements were performed, in addition to Raman scattering and visual inspection under a microscope. With these measurements, discussed in upcoming sections, the suitability of graphene for larger scale electrical devices and interfaces was determined.

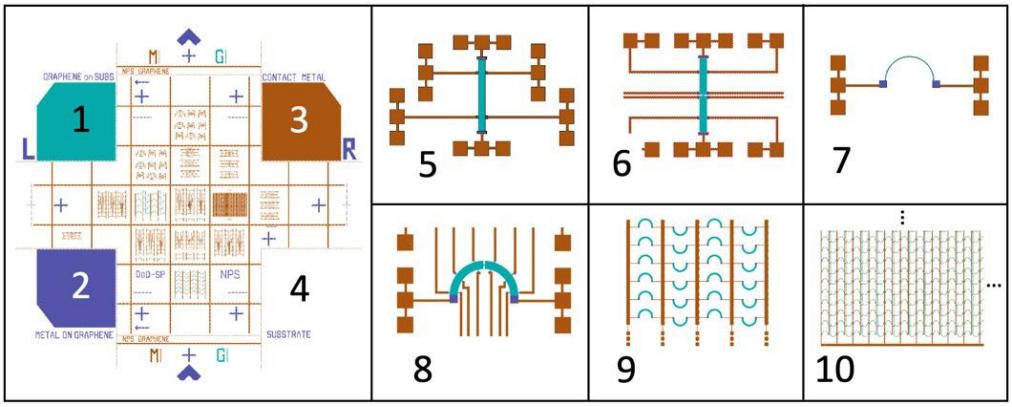

(1-4) Control areas of: graphene, contact metal on graphene, contact metal, and SiO_2 substrate, respectively. (5) A 100 µm x 1000 µm Hall Bar. (6) A 100 µm x 1000 µm Hall Bar with a 20 µm construction. (7) A 10 µm x 1000 µm arc. (8) A 100 µm x 1000 µm arc with a 20 µm constriction. (9) A 4 x 4 array of 100 µm x 1000 µm arcs. (10) Section of an 44x85 array of 5 µm x 100 µm arcs.

Figure 19. Mask layout and some of the fabricated structures

B. FABRICATION

Device fabrication begins with the commercially obtained CVD graphene wafers in the form of: 1 graphene/ SiO_2 (90 nm)/Si 4" p-doped and 1 graphene/hBN/ SiO_2 (285 nm)/Si 4" p-doped. A pair of 4" masks containing the device patterns including Hall Bars of assorted sizes and semicircular device geometries was used for both wafers.

The first mask was used to pattern the graphene into the desired device geometries. A layer of SPR-955-0.9 photoresist was spin coated onto each wafer followed by the pre-exposure bake. The respective wafers were then exposed to the mask pattern and then a post exposure bake. The wafers were then developed in a Microposit^{TM} CD-26 developer solution. Upon satisfactory developing, the wafers were then subject to an O_2 plasma reactive ion etch (RIE) to remove the unmasked graphene. After the RIE, the wafers were then subject to an acetone/isopropanol rinse to remove the remaining photoresist, leaving just the patterned graphene layer.

The second mask was used to pattern the metallic contacts that interface with the graphene devices via liftoff technique. As in the first mask, a layer of SPR-955-0.9 was spin coated onto each wafer followed by a pre-exposure bake. The wafers were then exposed to the mask pattern and then a post exposure bake. The wafers were then developed

in a CD-26 developer solution. Upon satisfactory developing, the wafers were placed in an Angstrom COVAP metal evaporator where a 5 nm adhesion layer of chromium (Cr) followed by a 50 nm layer of gold (Au) were deposited. The wafers were then placed in an acetone bath and subject to sonication for the liftoff process. At the conclusion of the liftoff process, the wafers were rinsed in deionized water and dried with compressed air. The wafers were then visually inspected and diced along 1 cm square grid lines. Diced areas that passed visual inspection—continuous graphene geometry, continuous metal contact—were then wire bonded to a 28 terminal ceramic dual inline package (CDIP28). An overview of the wafer processing is shown in Figure 20.

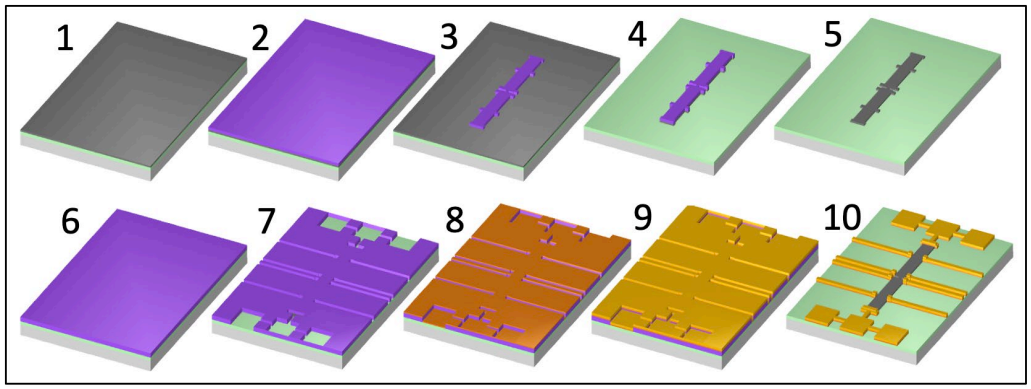

(1) 4" wafer with graphene on SiO2/Si or hBN/SiO2/Si. (2) Graphene patterning: deposition and exposure of photoresist layer with 1st mask. (3) Photoresist layer after developing of 1st mask pattern. (4) Removal of graphene in non-patterned areas with O2 plasma etch. (5) Acetone removal of 1st photoresist layer. (6) Metal patterning: deposition and exposure of photoresist layer with 2nd mask. (7) Photoresist layer after developing 2nd mask pattern. (8) Deposition of 5 nm Cr layer. (9) Deposition of 50 nm Au layer. (10) Liftoff of 2nd mask photoresist and excess metal.

Figure 20. Overview of the fabrication process

1. Raman Characterization

Prior to patterning, Raman spectroscopy [Figure 21] was performed to establish a quality baseline before and after the fabrication processes to verify the survivability of the graphene to the aggression of the O_2 plasma and acetone cleaning as well as photoresist contamination. A Renishaw inVia Raman microscope with a 514 nm wavelength laser at 50% power was used to obtain the Raman spectrum. The Spectrum data was acquired in

10 s sweeps for 300 accumulations. The measurements show strong presence of the identifying G peak and 2D peak and minimal presence of the disorder peaks D, D', and D+G. For quality graphene, the 2D/G and D/G ratios should be greater than 2 and near zero, respectively [71]. For the processed samples, the 2D/G and D/G ratios were calculated to be 4.709 and 0.103 for graphene on SiO_2 before etching and 4.336 and 0.159 after etching. These measurements indicate that while there is a change in quality after etching, it is not significant enough to expect adverse electrical performance.

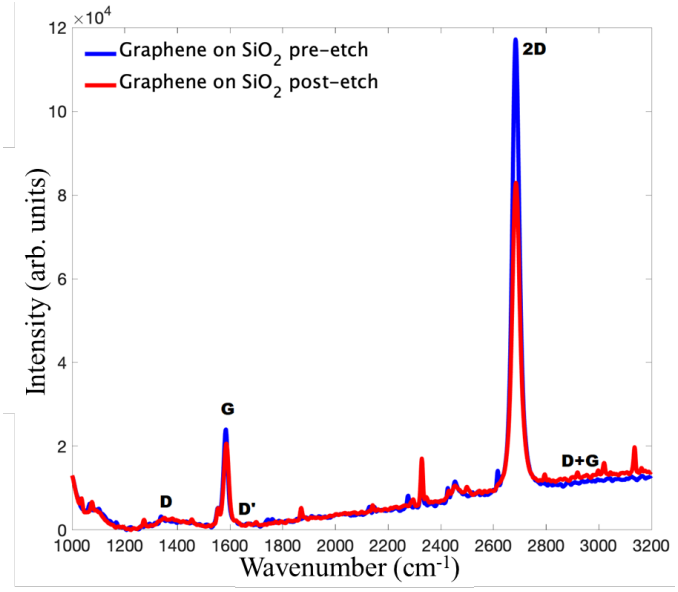

The identifying peaks: G (1580 cm^{-1}) and 2D (2690 cm^{-1}) are present. The disorder peaks: D(1350 cm^{-1}), D' (1620 cm^{-1}), and D+G (2940 cm^{-1}) are minimal.

Figure 21. Raman spectra of graphene on SiO_2 before O_2 plasma etch and after

2. Patterning Fidelity

A wide variety of geometries were patterned to determine the fidelity and robustness of the graphene patterning process at scale [Figure 22]. The mask design was organized in a grid with 1 cm x 1cm divisions allowing for redundant cells and redundant devices in the case of process defect, cleaving error, or mishandling. The device sizes ranged from 5 μm to 100 μm in width and 50 μm to 1000 μm in length in both rectangular

and semicircular geometries. Abrupt geometry changes in the form of constrictions in both rectangular and semicircular geometries were explored.

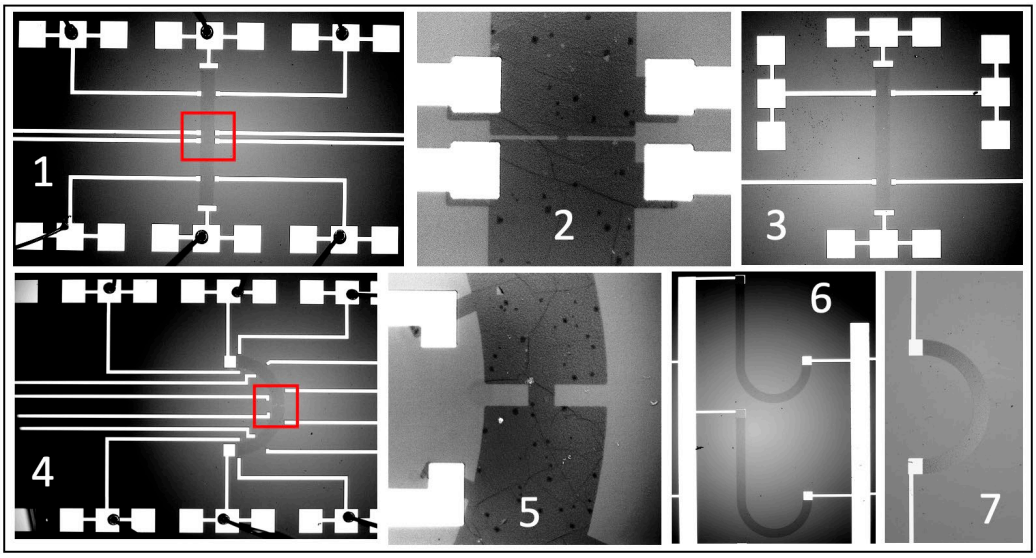

(1)A 100 μm x 1000 μm Hall Bar with a 5 μm constriction at 5x magnification. (2) 40x magnification of the 5 μm constriction from (1). (3) A 100 μm x 1000 μm Hall Bar at 5x magnification. (4) A 100 μm x 1000 μm arc with a 20 μm constriction at 5x magnification. (5) 40x magnification of the 20 μm constriction from (4). (6), (7) 100 μm x 1000 μm arc elements of a 4x4 array at 5x magnification.

Figure 22. Fabricated devices

A visual inspection of the wafers indicates that the mask patterns are transferred to the graphene with high fidelity for feature sizes as small as 5 µm. This is evident as the semicircular features maintain their curvature along the inner and outer edges as well as the sharp corners present in the constricted geometries. The device patterns remain continuous for the largest features up to 1000 µm and the device arrays demonstrate the repeatability device fidelity over large areas approaching 1 cm^2.

C. CONDUCTIVITY MEASUREMENTS

Having demonstrated that the graphene can be patterned with conventional photolithography over a large area with features ranging from 5 µm to 1000 µm device electrical properties were then measured. For the remainder of this section, the 100 µm ×

1000 µm Hall bars on both substrates will be examined. Initial electrical characterization by 2-point and 4-point probe was performed on a Keysight B1500A semiconductor device analyzer at room temperature. Sheet resistance of the 100 µm × 1000 µm Hall Bar on both SiO_2 and hBN were within 450 ± 5 Ω/sq. This is within the manufacturer's specification of 430 ± 50 Ω/sq [51]. Contact resistance for the longitudinal pair was 7.7 kΩ for graphene on SiO_2 and 5.5 kΩ for graphene on hBN/SiO_2. The resistance measurements indicate that Ohmic contact was achieved at the graphene/metal interface.

1. Charge Neutrality Point

The location of the charge neutrality point (CNP) [46] for each device was then determined by applying a constant DC bias of 1 V along the length of the Hall Bar and applying a backgate voltage sweep from 0 V to 100 V and back. The backgate sweeps [Figure 23] indicate that there is hysteresis and the CNP location is direction dependent. For the graphene on SiO_2 device, the CNP is located at 40 V in the forward direction and 50 V is the backward direction. For the graphene on hBN/SiO_2 device the CNP is located at 55 V in the forward direction and 75 V in the backward direction.

As described by [46], the terms Dirac point and CNP are often interchanged in the literature as they do describe the same condition—where the Fermi energy, E_{Fermi}, is zero—there is an important distinction to be made. In theory, at the Dirac point no current should flow as there are no charge carriers available given by graphene's dispersion relation and consequently the resistance should be infinite. The measurements instead show that the resistance achieves a finite peak. At this point of maximum resistance, the number of intrinsic carriers has reached its minimum and concentration of electrons and holes are equivalent—charge neutrality. Under ideal circumstances the resistance versus backgate voltage plot assumes a Gaussian shape with holes being the dominant carrier at voltages less than the CNP and vice versa for electrons. The hysteresis is due to charge trapping in the oxide layer as the gate voltage swept. The broadening of the trace is due to impurities and charge trapping in at the top and bottom of surfaces of the graphene. The graphene on SiO_2 shows a particularly broad trace past at voltages over the CNP indicating that the charge traps and impurities on this sample have an affinity for electrons [72].

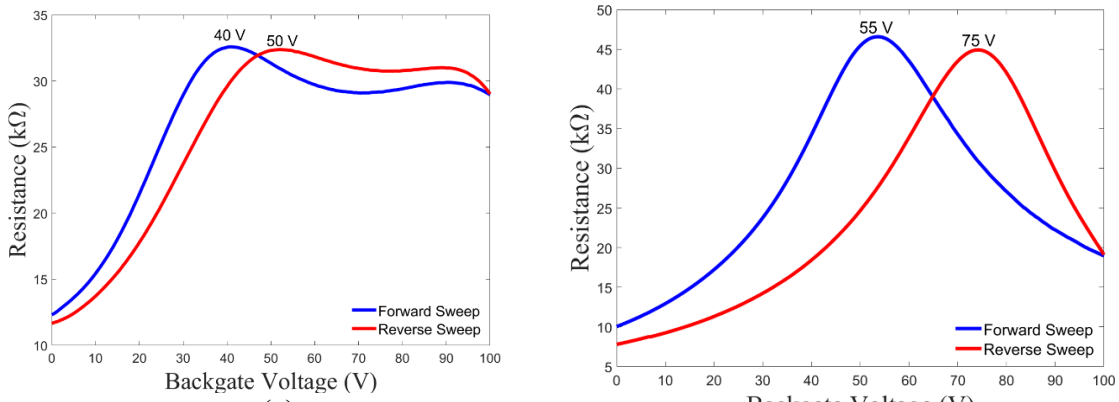

Backgate sweeps to locate the charge neutrality point for (a) graphene on SiO_2 and (b) graphene on hBN/SiO_2.

Figure 23. Charge neutrality point plot

2. Hall Effect Measurements

Hall effect measurements were then performed on both devices with a Leybold Hall Effect apparatus at room temperature with no backgate applied. The devices were subject to a magnetic field ranging from 20 mT to 136 mT [Figure 24]. Measurements for the graphene on both substrates were performed at two currents: 0.028 A and 0.2 A. The Hall effect coefficients (R_H) were calculated to be 1.435×10^{-11} m^3/C for graphene on SiO_2 and 1.365×10^{-8} m^3/C for graphene on hBN/SiO_2.

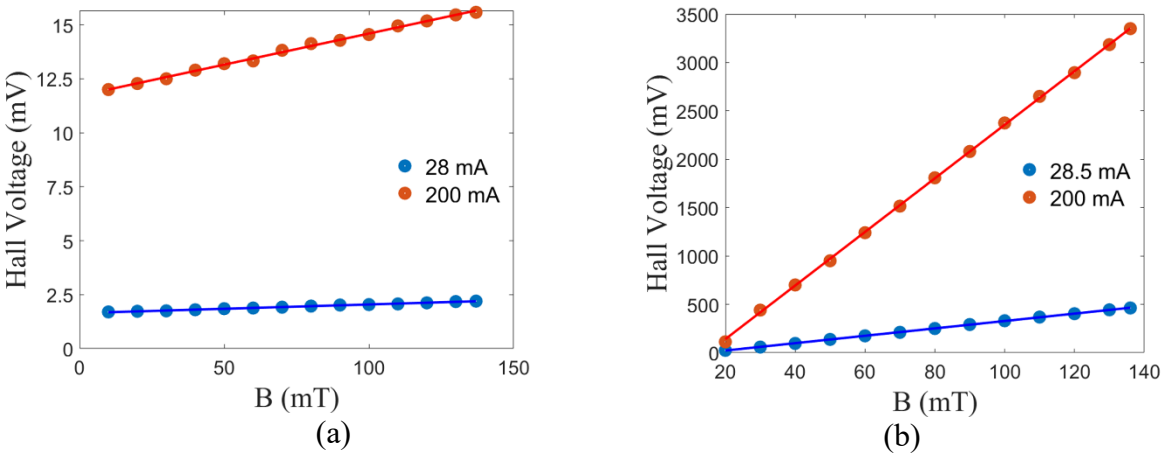

Hall Effect measurements for (a) graphene on SiO2 and (b) graphene on hBN/SiO2.

Figure 24. Hall effect measurements

3. Quantum Conductance and Minimum Conductivity

With the devices characterized, more in-depth device properties can be assessed. Having determined the charge neutrality point and the maximum device resistance, the minimum device conductivity in terms of the conductance quantum [73] ($G_0=2e^2/h$) is calculated [Figure 25]. Graphene on SiO_2 has a minimum conductivity of ½ G_0 while graphene on hBN/SiO_2 has a minimum conductivity of ¼ G_0.

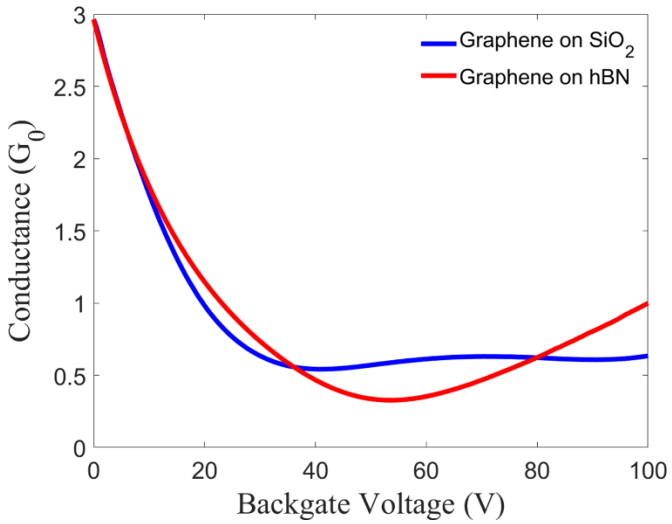

Device conductance in units of the quantum of conductance for graphene on SiO_2 and graphene on hBN/SiO_2.

Figure 25. Device quantum conductance

Using the measured Hall coefficients, the carrier density of the devices was calculated with the relation:

$$n = \frac{1}{eR_H} \tag{14}$$

where e is the electron charge and R_H is the Hall coefficient [74]. For the graphene on SiO_2 the carrier density is 4.35×10^{29} m^{-3} while graphene on hBN/SiO_2 has a carrier density of 4.6×10^{26} m^{-3}. The carrier mobility can then be determined with the relation:

$$\mu = \frac{1}{en\rho} \tag{15}$$

where ρ is the resistivity. The carrier mobilities are 3.5 $cm^2/V\cdot s$ and 3×10^3 $cm^2/V\cdot s$ for graphene on SiO_2 and graphene on hBN/SiO_2, respectively. Accounting for the minimum conductivity of graphene, a modified mobility expression [75] is as follows:

$$\mu = \frac{\sigma - \sigma_0}{en} \tag{16}$$

where σ is the device conductivity and σ_0 is the device minimum conductivity. With the corrections the mobilities are now 2.6 $cm^2/V \cdot s$ and 2.68×10^3 $cm^2/V \cdot s$ for graphene on SiO_2 and graphene on hBN/SiO_2 respectively.

D. ANALYSIS

While the fabricated devices are designed to be identical, the electrical and Hall Effect characterization indicate that the graphene is highly affected by the insulating material it resides on. Starting with the resistance and CNP sweeps [Figure 23], the graphene on SiO_2 has a very broad shape perhaps even bimodal while the graphene on hBN is well shaped and nearly Gaussian. The broadening of resistance curve is due to the presence of impurities [46]. Hall effect measurements show that graphene on hBN/SiO_2 is 3 orders of magnitude more responsive to an applied magnetic field. These 3 orders of magnitude difference carries through in the carrier density difference and the carrier mobility difference. Graphene on SiO_2 behaves like a lightly doped semiconductor in terms of its carrier density (7.8×10^{15} cm^{-2}), but more like a metal in terms of its mobility. The low mobility of graphene on SiO_2 is mostly attributed to phonon scattering [58]. Graphene on hBN/SiO_2 agrees with other works in terms of Hall response, carrier density (8.2×10^{12} cm^{-2}). At this length scale, the graphene on hBN/SiO_2 mobility of 2.68×10^3 $cm^2/V \cdot s$ is comparable to that of GaAs [76]—a common high mobility semiconducting material. Both CNP measurements and Hall effect measurements indicate that both devices are hole dominant transport. This was expected as both graphene devices reside on p-doped Si.

Interestingly, the graphene on SiO_2 did have a higher minimum conductance (½ G_0) than graphene on hBN/ SiO_2 (¼ G_0). This is due to the presence of impurities providing charge carriers despite the applied back gate depleting the device of intrinsic carriers from the graphene. In both cases the minimum conductance is a fraction of G_0 suggesting that ballistic transport does not occur in either of these devices [14], [58]. This result is also expected since the device length of 1000 μm exceeds the manufacturer's specification of ~10 μm grain size. Charge carriers in these devices will inevitably encounter scattering at the grain boundaries as they traverse.

The possibility of creating large scale repeatable device patterns with conventional photolithography on commercially obtained CVD graphene wafers residing on either SiO_2 or hBN/SiO_2 has been demonstrated. The pattern fidelity is high enough to where semicircular shapes maintain their curvature and abrupt geometry changes are produced without noticeable edge rounding. This method can accommodate device elements as small as 5 µm and as large as 1 mm. While both substrates were continuous and conductive on a 1 mm scale, graphene on hBN/SiO_2 had mobilities on the order of 10^3 $cm^2/V{\cdot}s$ which is comparable to existing high mobility semiconductor materials. Depending on cost or application, CVD graphene on an appropriate insulator shows promise as a modern electronics foundation. For the purpose of implementing a cyclotron style device, CVD graphene on hBN/SiO_2 should be selected due to its high mobility.

With the above measurements, the saturation velocity can be extracted using a method from [66] using the relation:

$$v_d(E) = \frac{\mu E}{\left[1 + \left(\frac{\mu E}{v_{sat}}\right)^{\gamma}\right]^{1/\gamma}} \tag{16}$$

where v_d is the measured drift velocity, μ is the carrier mobility, E is the applied electric field magnitude, and γ is a fit parameter. At room temperature conditions this can be simplified to [42], [77]:

$$v_{sat} \approx \frac{2\omega_{OP}}{\pi\sqrt{\pi n}} \tag{17}$$

where $\omega_{OP} = {}^{102\,meV}/_{\hbar}$ is the optical phonon energy at room temperature, and n is the charge density. A value of $1.87{\times}10^7$ cm/s, is obtained which is similar to the velocity $2{\times}10^7$ cm/s used by other researchers [16]. This saturation velocity is significantly different from the value used for the performance estimations in section II. The measurement-derived saturation velocity was then used to produce updated simulations.

The series of simulations from section II were repeated on the 6.7 GHz (10 µm radius) design. For a 10 µm radius, the target frequency is now 2.9 GHz with a peak power based on the analytic model occurring at 3.94 GHz [Figure 26]. Like with the previous efforts, the analytical model gives the highest value for the peak, followed by the FE arc at 3.85 GHz, and the FE dipole at 3.74 GHz. Consequently, the peak to target ratios [Table 3] follow the same trend and closely track with the results in Table 2.

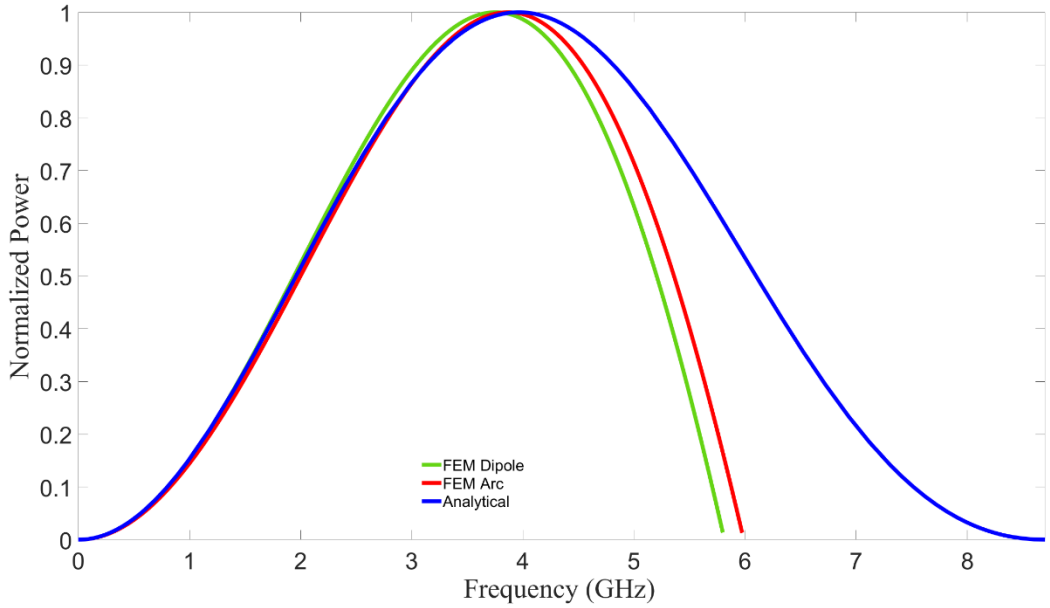

Updated frequency spectrum for the 10 µm arc radius design with all models plotted together. The target frequency is now 2.9 GHz, down from 6.7 GHz.

Figure 26. Updated simulated frequency spectrum

Table 3. Peak to target frequency ratio: 2.9 GHz target

Model	Peak to target frequency ratio
Analytical	1.36
FE Dipole	1.29
FE Arc	1.34

Power output is expected to be in the range of 3.96 nW±47%. As shown in Table 4, the expected power calculated by the Larmor method exceeds that of the other methods by a factor of nearly 2.

Table 4. Power tabulation for 2.9 GHz target frequency

Model	**Power (nW)**
Larmor	6.095
FE Dipole	3.171
FE Arc	2.617

IV. RADIATION TESTING WITH MICRON SCALE DEVICES

With simulations and preliminary characterization of graphene on hBN complete, attempts to experimentally demonstrate cyclotron radiation from graphene can proceed. The fabrication process is virtually identical to the process in Chapter III, with the mask contents being the only difference. With respect to tooling, the previous fabrication series utilized a thermal evaporator (Angstrom COVAP) to deposit the metal layers. For this fabrication series, the films were deposited by sputtering (Angstrom NEXDEP). During the packaging process, it was found that the sputtered metal films were incompatible with the wire bonding process. To make the final connections, silver paste was applied between the desired conductive elements. For this fabrication series, the entire wafer will function as a single device unlike in the previous fabrication series in which the wafer was diced and packaged into a 28 pin CDIP.

A. DESIGN AND FABRICATION OVERVIEW

The intent of this design is to populate as much of the usable area of the 4" wafer with the 10 μm arc radius design in the unit cell configuration in [Figure 27 (a)]. A 20 μm wide interconnect of Cr/Au encapsulates the graphene except for the active radiating areas. The encapsulated design was opted for even though the measurements from section III suggest that monolithic interconnects are possible. To achieve large scale arrays the resistivity properties of Au (0.44 Ω/sq [22]) is more desirable than that of graphene (450 Ω/sq). Encapsulation also mitigates high contact resistance common with metal/graphene interfaces [78]–[80].

The active radiating areas of the unit cell [Figure 27 (a)] consists of the familiar semicircular arc with an adjacent "J" shaped arc. By reversing the direction of the adjacent arc, the central metallic interconnect can be shared while preserving the rotation for both arcs. An additional straight graphene patch with length equivalent to πr_{arc} is also added to form a "J" shaped arc to introduce a π phase delay. The introduction of the phase delay should prevent simultaneous emission from both arcs which may result in destructive interference.

The unit cell— measuring 160 µm × 100 µm— is repeated to make a 129 × 70 unit stack [Figure 27 (b)]. A column is then formed by reflecting a stack about the horizontal centerline of the wafer with a 1.2 mm space between the stacks, which are connected by wire bonding post fabrication. The central region of the wafer is populated with a total of 8 columns. The columns are then connected to a large bus bar that spans the width of the wafer to interface with instrumentation. In total, the designed wafer layout contains 288,960 arcs [Figure 27 (c)]. Such a large number of arcs is desired to effectively multiply the output of a single arc and increase the chances of detection. This is also helpful in providing redundancy in the case of defects from the fabrication process, environmental contamination, or breakage.

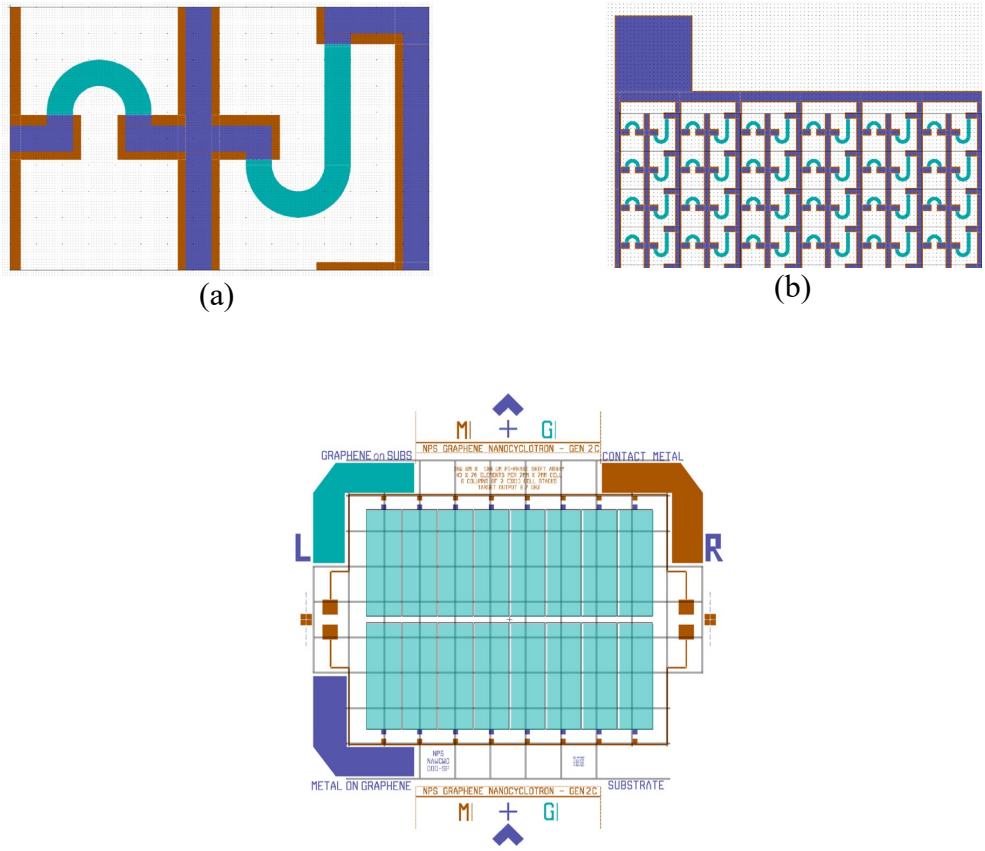

(a) Array unit cell consisting of a semicircular arc and an inverted arc with π phase delay to make a "J" shape. (b) Top right corner of an array column. (c) Mask layout consisting of 8 columns straddled by 2 bus bars with 3 mm x 3mm contact pads on each side.

Figure 27. Array unit cell, stack, and wafer

As part of the experimental process, a reference wafer was fabricated from a previously successful wafer process by subjecting the wafer to an additional O_2 plasma etch for 20 seconds. This would remove the exposed graphene in the active radiating areas and leave only the metallic network. A comparison between the emissions of the two wafers will distinguish which emissions are due to the metallic network and which emissions are due to the graphene.

B. PACKAGING AND CHARACTERISTICS

Following cleanroom fabrication, a 30 cm coaxial cable with SMA interface was spliced and soldered to the large metallic contacts on the lefthand side of the wafer. The wafers were then packaged in custom designed 3D printed plastic enclosures as shown in Figure 28.

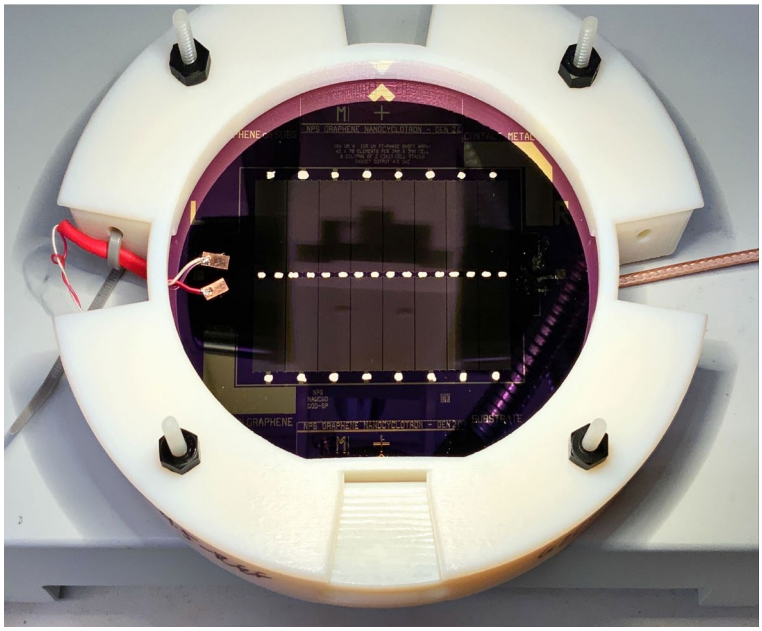

Post fabrication packaging of the 4" wafer. Electrical contact between the columns and the bus bars are made via conductive silver paste. A spliced coaxial cable is soldered to the large contact pads on the bus bars.

Figure 28. Packaged wafer

DC characterization tests using the semiconductor device analyzer found that the total wafer resistance is 7.75 kΩ. For the reference wafer, DC characterization tests resulted in open circuit readings thus verifying that the second round of RIE removed the exposed graphene. Following the DC characterization of the wafers, preliminary RF characterization was conducted in the form of a scattering parameter (S_{11}) measurement—also known as return loss—using an Agilent N5222A vector network analyzer (VNA) [Figure 29]. This characterization method applies a fixed input power to the sample over a span of frequencies and measures the returned power from the same device port.

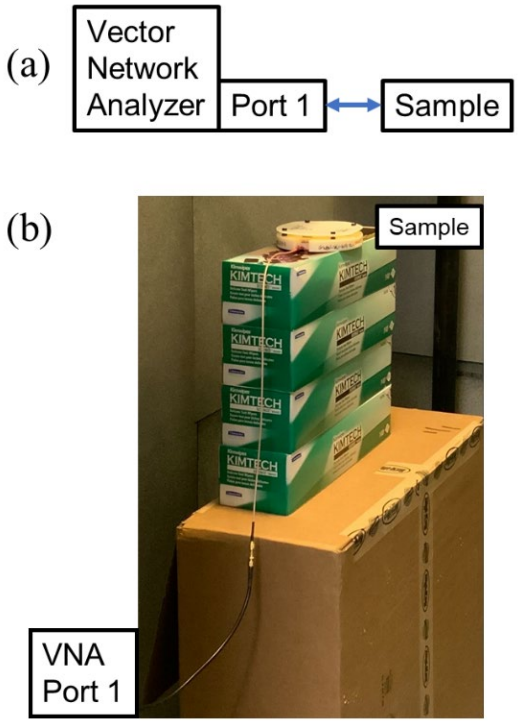

(a) S_{11} characterization begins with stimulus from the VNA's port 1 applied to the sample. The VNA then records the returned power for each frequency in the desired sweep range. (b) A fabricated sample undergoing an S_{11} measurement.

Figure 29. S_{11} diagram

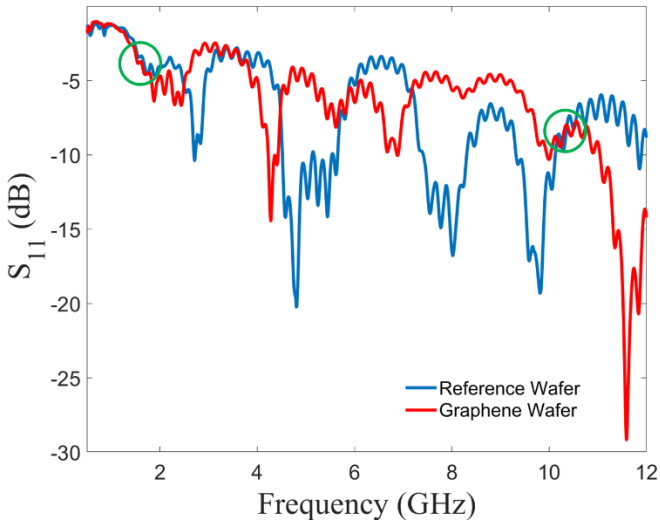

Scattering parameter measurement (S_{11}) of the graphene (red) and reference (blue) wafers. For testing, it was necessary to find a stimulus frequency away from the target frequency where both graphs intersect (green circles): 1.73 GHz and 10.16 GHz.

Figure 30. S_{11} measurements

To demonstrate the cyclotron radiation process, the wafer requires stimulation away from the target frequency. To make a fair comparison, both the reference and graphene wafer were stimulated at a frequency where their S_{11}s are the same [Figure 30] as this assumes that both the reference and graphene wafers will receive the same power. These frequencies were determined to be 1.73 GHz and 10.24 GHz with S_{11}s of -4.44 dB and -8.96 dB, respectively. These S_{11}s fall below the general standard of -10 dBm (10% of incident power reflected). A matching network can be implemented to improve the respective S_{11}s; however, the additional task of doing so was neither possible under time and resource constraints nor seen as valuable as the selected frequencies already met the fairness requirements. The matching network may also inadvertently bias the emissions that are being investigated towards the matching frequency. This step is rather important when practical devices are being implemented.

In addition to the S_{11} measurement, another scattering parameter (S_{21})—also known as insertion loss—was measured using an Agilent FieldFox N9918A VNA. This characterization method applies a fixed input power, from port 1, to the sample over a span of frequencies and measures the transmitted power, after propagating through free space, via horn antenna (AS-48461) connected at port 2 [Figure 31]. A separation distance of 47 cm from the sample to the receive horn antenna was chosen as this is the minimum distance to achieve the far field condition at the highest expected frequency of 6 GHz. The S_{21} measurements served as the first indication if the sample radiates and can reveal any polarization dependencies of the emissions. Horizontal and vertical polarizations were obtained by rotating the horn antenna by 90°, with the vertical polarization defined as the horn elements parallel to the length of the wafer's columns. The S_{21} measurements were performed at room temperature in an anechoic chamber lined with RF absorbent material hosted by the Airborne Instrumentation Systems Department at NAWCWD–Point Mugu.

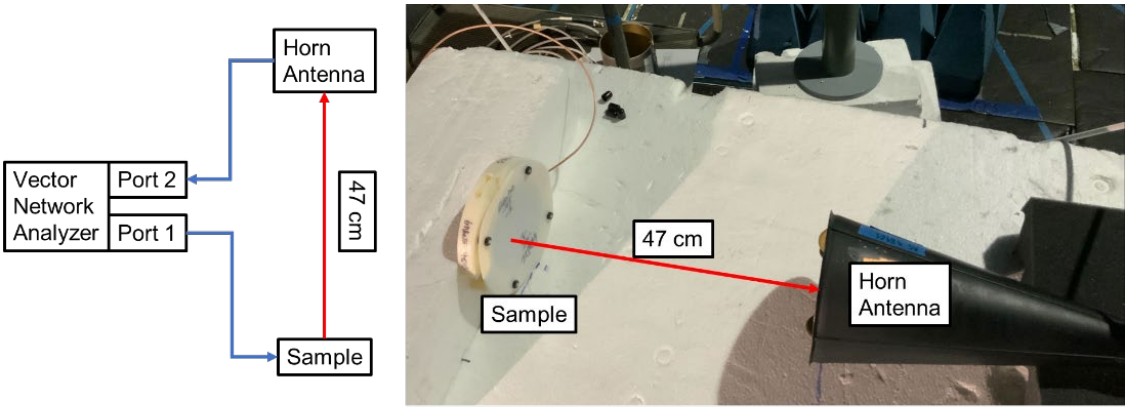

(a) (b)

(a) S_{21} characterization begins with stimulus applied from VNA port 1 to the sample. Emissions propagate through free space which are received by a horn antenna connected to VNA port 2. (b) A fabricated sample undergoing an S_{21} measurement.

Figure 31. S_{21} diagram

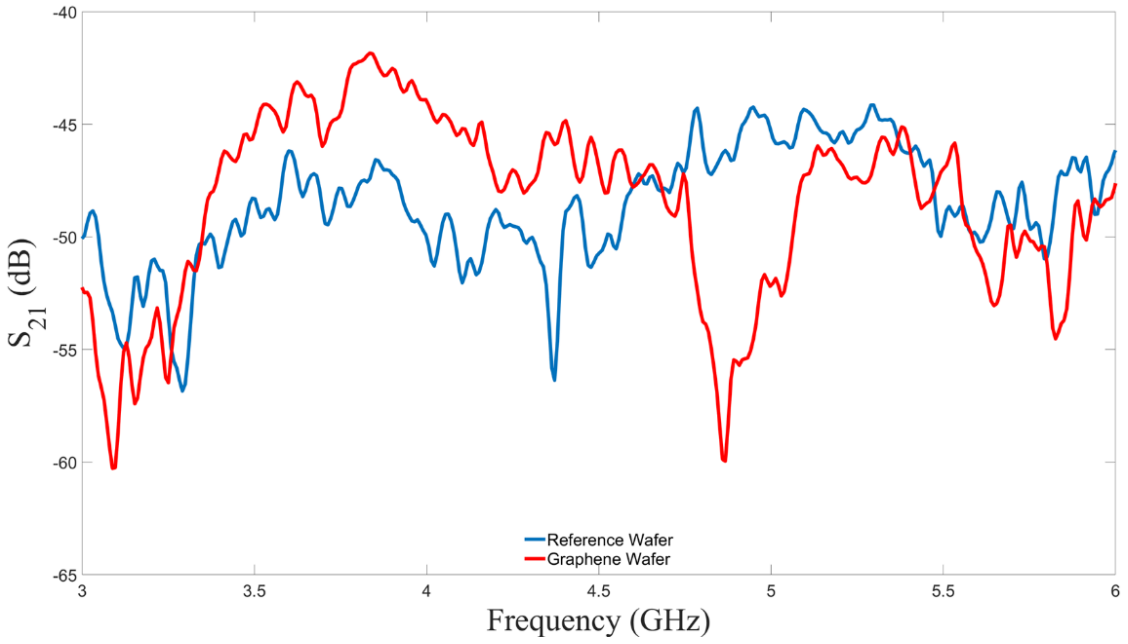

Figure 32. S_{21} measurement: Vertical polarization

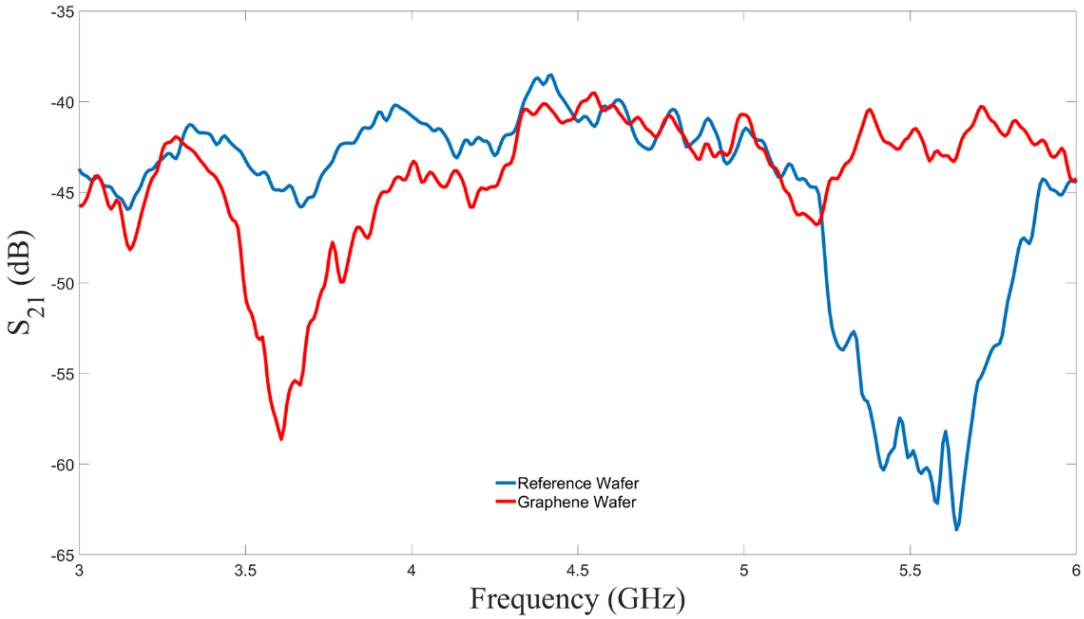

Figure 33. S_{21} measurement: Horizontal polarization

With the S_{21} measurements completed, some additional insights into the characteristics of the wafers have been revealed. For both polarizations, both wafers radiated across the span of 3 GHz to 6 GHz above the instrument's detection threshold of -65 dB. Furthermore, a distinction between the polarization modes has been demonstrated. For the vertical polarization [Figure 32], the graphene wafer transmitted more power than the reference wafer from 3.4 GHz to 4.5 GHz. For the horizontal polarization [Figure 33], the opposite was observed in which the reference wafer transmitted more power over the same range. Going forward, the S_{21} results assisted in the expectations and interpretations of the band conversion measurements.

C. METHODS

Band conversion measurements were performed at room temperature in an anechoic chamber lined with RF absorbent material hosted by the Physics Department at NPS. The samples were placed at 47 cm from the receive horn antenna (AEL H-1498) as this is the minimum far field distance for 6 GHz propagation—the upper frequency limit from the simulations. In the resulting measurements, the vertical polarization was defined as the horn elements parallel to the length of the wafer's columns. The horizontal

polarization was obtained by rotating the sample 90 degrees. A 10-foot coaxial cable connects the antenna to a 20 dB low noise amplifier (RF Bay LNA-8G) followed by a 3-foot coaxial cable connected to an Agilent E4407B spectrum analyzer.

Stimulus was provided by an HP 8350B signal generator, connected by a 3-foot coaxial cable to a variable attenuator (-50 dB to 0 dB, 10 dB step). Another 3-foot cable connects the variable attenuator to a power amplifier (QPJ-02183050). Lastly, a 6-foot cable from the power amplifier connects to the wafer. A schematic of the testing apparatus is shown in Figure 34.

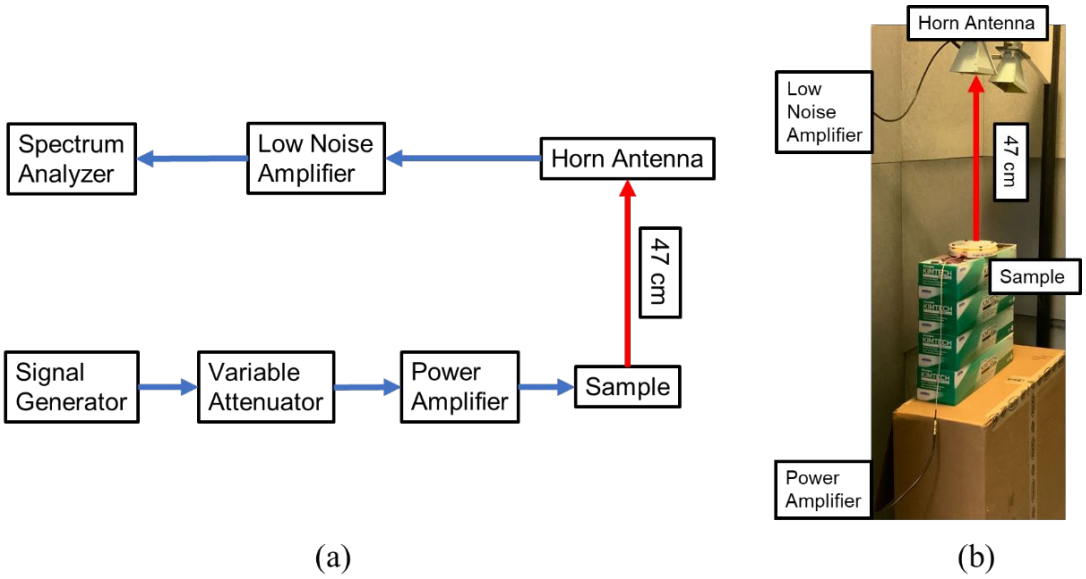

(a) Diagram of band conversion characterization. Stimulus is provided by a signal generator whose output is routed through a variable attenuator and a power amplifier before connecting to the sample. Emissions from the sample are incident on a horn antenna which feeds into a low noise amplifier. The received amplified signal is then fed into the spectrum analyzer for measurement and recording. (b) A sample undergoing band conversion characterization in the anechoic chamber.

Figure 34. Band conversion characterization diagram

D. PROCEDURE

Testing began with a 30-minute warmup of the test apparatus (signal generator/amplifier/spectrum analyzer). After the warmup, a background collection was performed for both the reference and the graphene wafers. Each data collection consisted

of a 8192 sample power average of 1001 points from 1 GHz to 12 GHz in broad spectrum collection and 3 GHz to 6 GHz for fine spectrum collection. Following the background collection, emissions were collected by starting at the sub-target stimulus frequency and sweeping though the input power range, followed by super-target stimulus frequency. This process was repeated for each polarization for each wafer. The test procedure was as follows:

A. Broad Spectrum (1 GHz–12 GHz)

    a. Reference wafer:

        Place reference wafer in chamber and connect to source cable in the vertical polarization position.

    b. Vertical polarization:

        i. Collect background

        ii. Collect emissions with low frequency stimulus applied (1.73 GHz) at the following powers (measured at the input of the sample): 15 dBm, 20 dBm, 27 dBm, and 30 dBm.

        iii. Collect emissions with high frequency stimulus applied (10.16 GHz) at the following powers (measured at the input of the sample): 10 dBm, 15 dBm, and 20 dBm.

    c. Horizontal polarization:

        Rotate the wafer 90° and repeat procedure b.

    d. Graphene wafer:

    Replace the reference wafer in chamber with the graphene wafer and connect to source cable in the vertical polarization position and repeat procedures b through c.

B. Fine Spectrum (3 GHz–6 GHz)

    a. Reference wafer:

Place reference wafer in chamber and connect to source cable in the vertical polarization position.

b. Vertical polarization:

   i. Collect background.

   ii. Collect emissions with low frequency stimulus applied (1.73 GHz) at the following powers (measured at the input of the sample): 20 dBm and 27 dBm.

   iii. Collect emissions with high frequency stimulus applied (10.16 GHz) at the following powers (measured at the input of the sample): 15 dBm and 20 dBm.

c. Horizontal polarization:
   Rotate the wafer 90° and repeat procedure b.

d. Graphene wafer:
   Replace the reference wafer in chamber with the graphene wafer and connect to source cable in the vertical polarization position and repeat procedures b through c.

Raw data of the graphene wafers for the broad spectrum collections are plotted in Figure 35. Due to the presence of harmonics and saturation of the power amplifier, the 30 dBm measurements were deemed not insightful for measuring under fine spectrum. The broad spectrum collections also justify the truncation of the fine spectrum to the 3 GHz to the 6 GHz range as the sub 3 GHz range contains excessive spurious emissions while no significant emissions are detected at over 6 GHz.

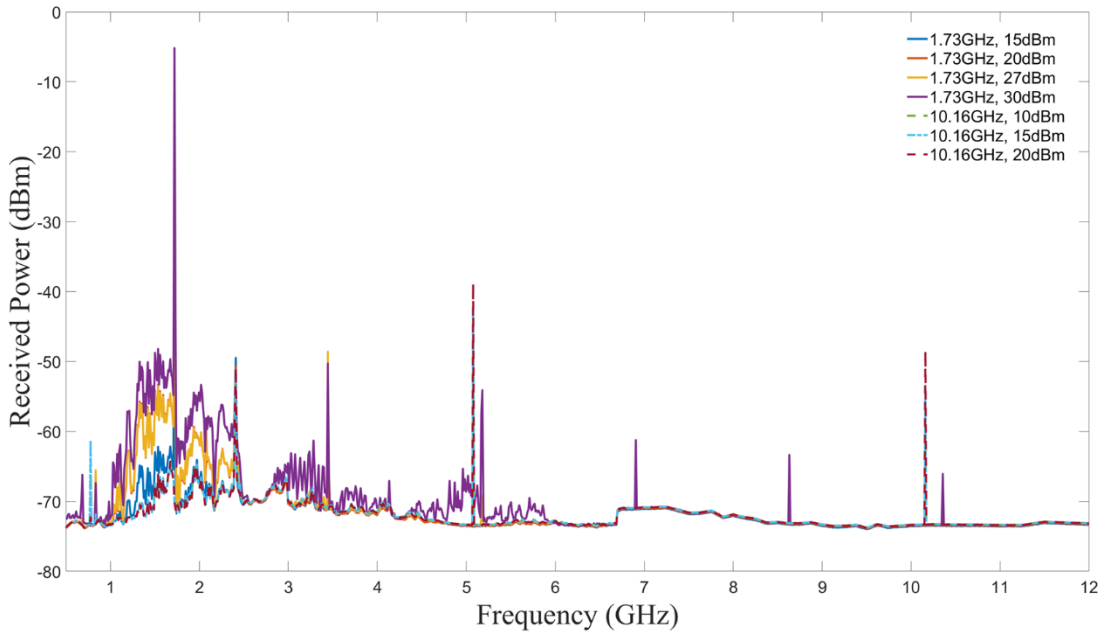

(a)

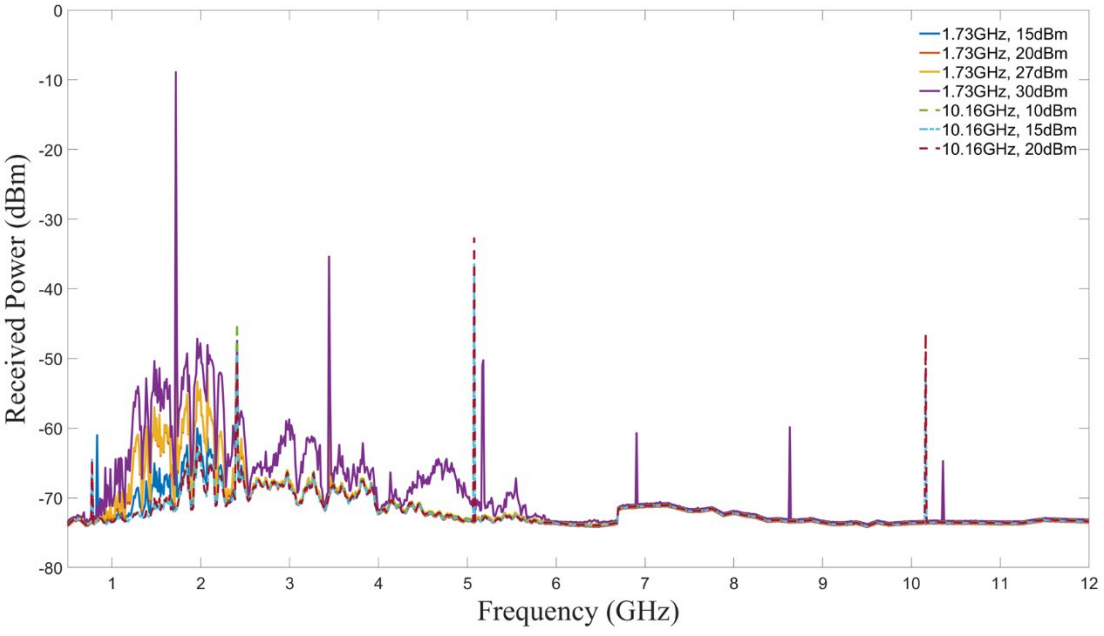

(b)

Broad spectrum emissions data (a) vertical polarization (b) horizontal polarization

Figure 35. Broad spectrum emissions

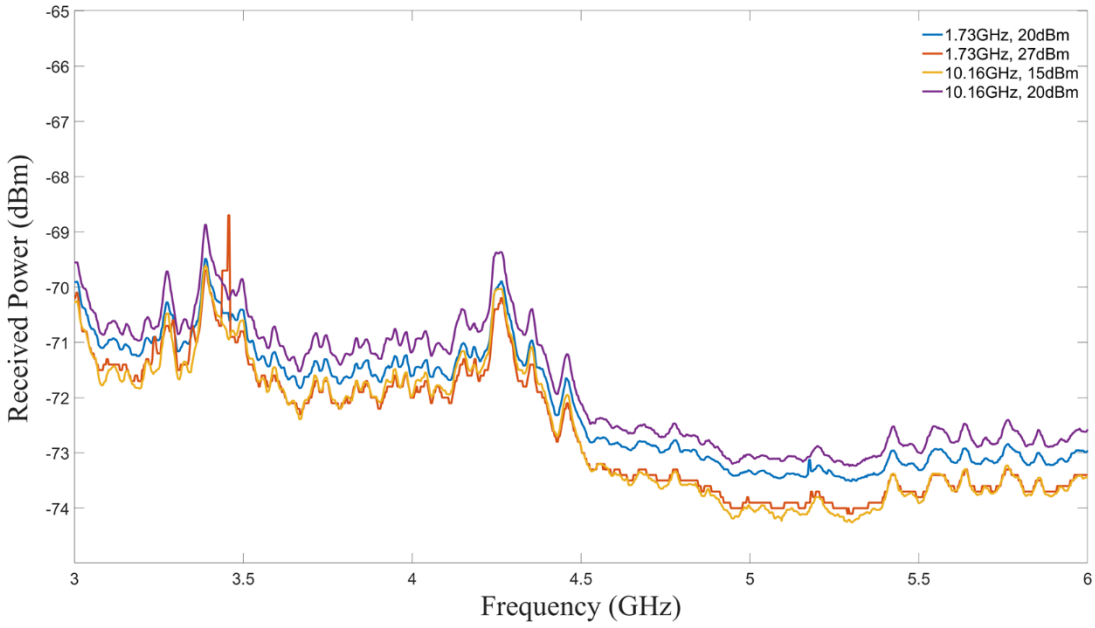

(a)

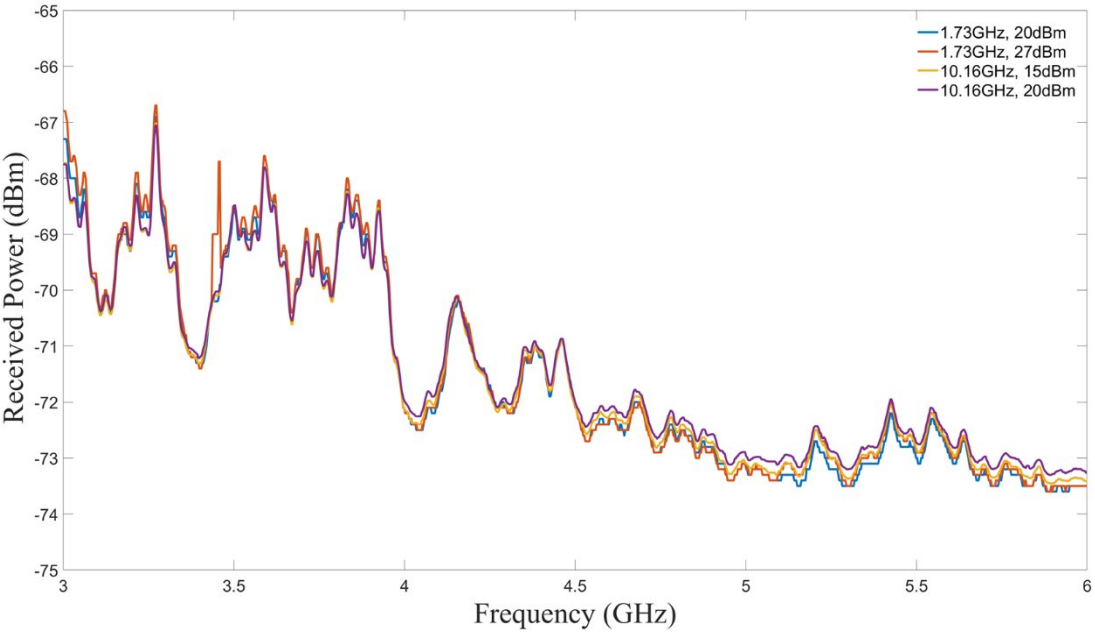

(b)

Fine spectrum emissions data (a) vertical polarization (b) horizontal polarization

Figure 36. Fine spectrum emissions

With the fine spectrum emissions, the behavior of the device at the intended design range starts to appear. In Figure 36, it is observed that all traces are within 1 dB of each other. Emissions from the horizontal polarization were more tightly grouped than the vertical polarization indicating that the emissions were mostly due to the metallic network as the metallic was more uniformly fabricated than the graphene. This non-uniformity in the graphene was mostly due to the grain formation which is an inherent characteristic of CVD grown graphene [45]. This observation was consistent with the S_{21} measurements for the horizontal polarization (Figure 33), where the metallic network was the dominant emissions source.

The emissions seem to be independent of the input stimulus frequency and power. If these emissions are due to the cyclotron radiation, it is likely that only the same number of elements are contributing to the radiation. Figure 37 shows the signal, reference, and background data with a stimulus of 1.73 GHz at 20 dBm power.

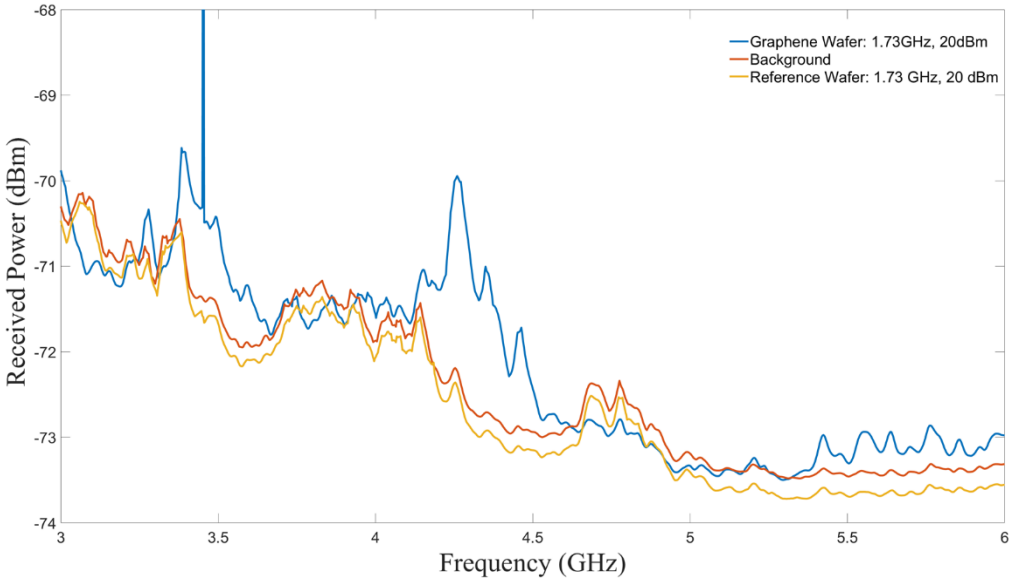

(a)

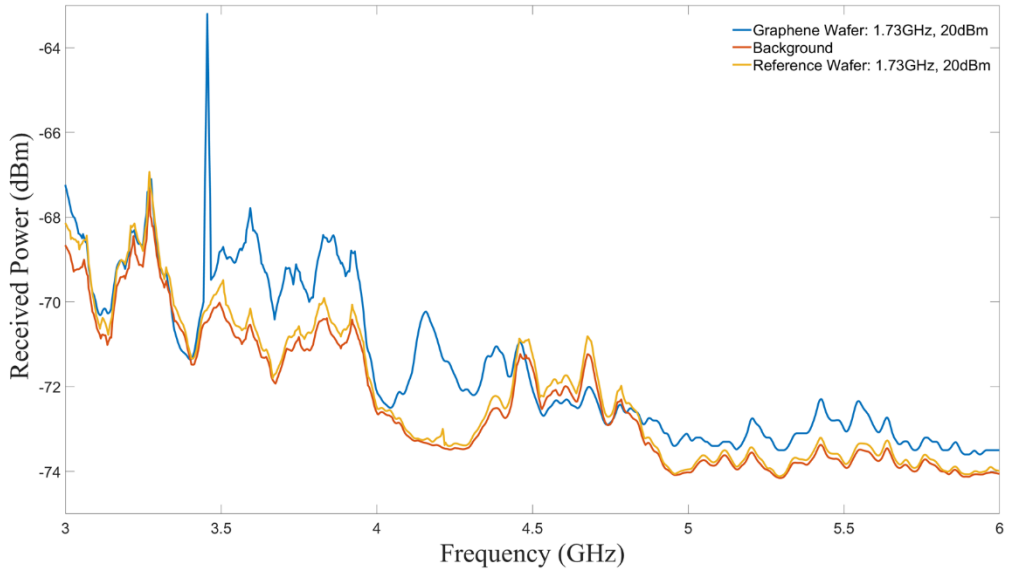

(b)

(a) Vertical Polarization (b) Horizontal Polarization

Figure 37. Signal, reference, and background

E. ANALYSIS

With the raw data collected, analysis was performed in the form of signal-to-noise ratio (SNR) and signal-to-reference ratio (SRR). Harmonics were also removed from the data. SNR was obtained by subtracting the background data from the applied stimulus data. This provides insight into whether there is a net emission from the device.

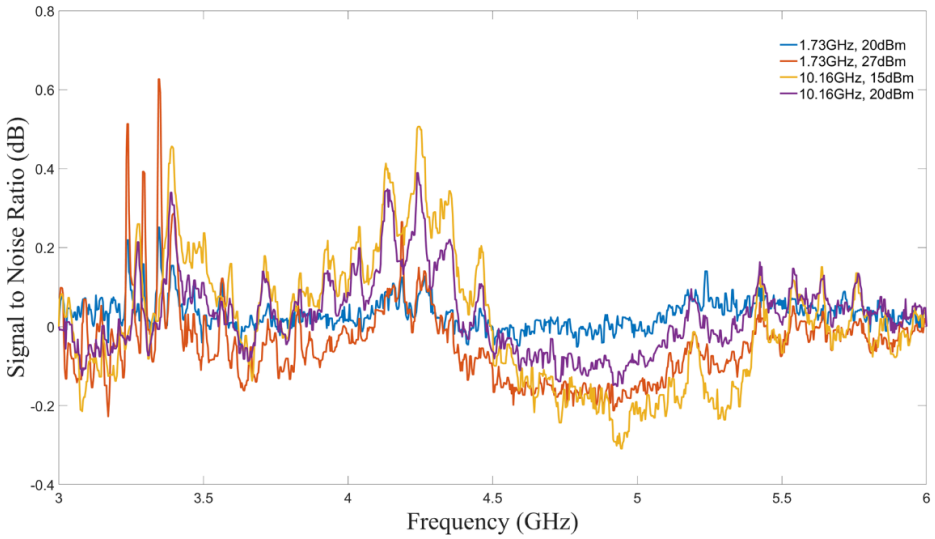

(a)

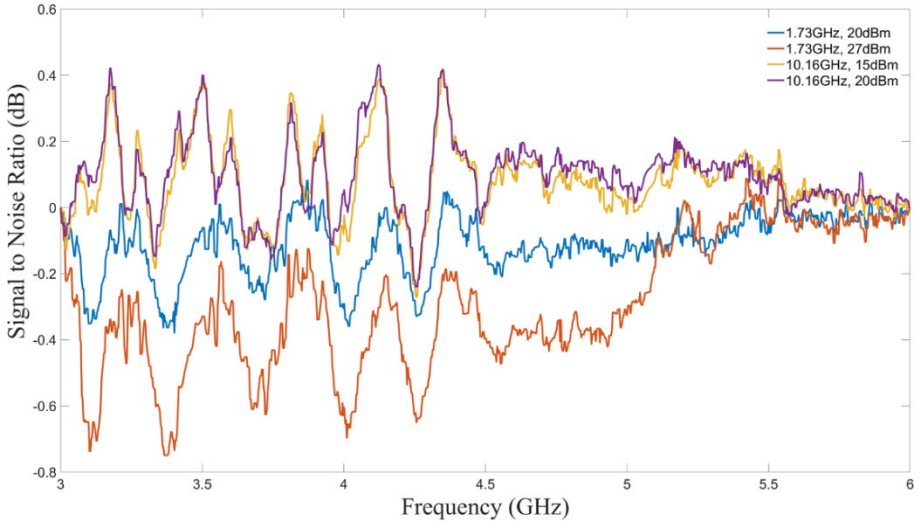

(b)

(a) Vertical Polarization (b) Horizontal Polarization

Figure 38. Signal to noise ratio

As shown in Figure 38, the measured SNR is extremely low indicating that the cyclotron emissions are at the same level of the noise or nonexistent with this experiment method. There were even cases where the signal is below the noise level. This was likely due to a drift in the sensitivity of the test equipment as each sampling required 40 minutes to complete. With SRR, the reference emission data was subtracted from the graphene emission data. To access the such small signals, the SRR was used. Any net positive readings would be due to the presence of the graphene resulting from cyclotron style emissions.

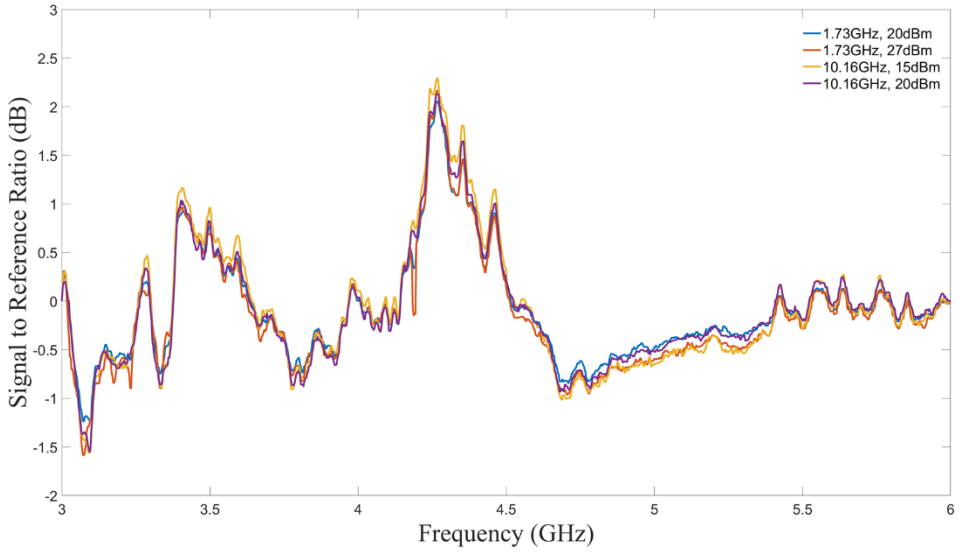

(a)

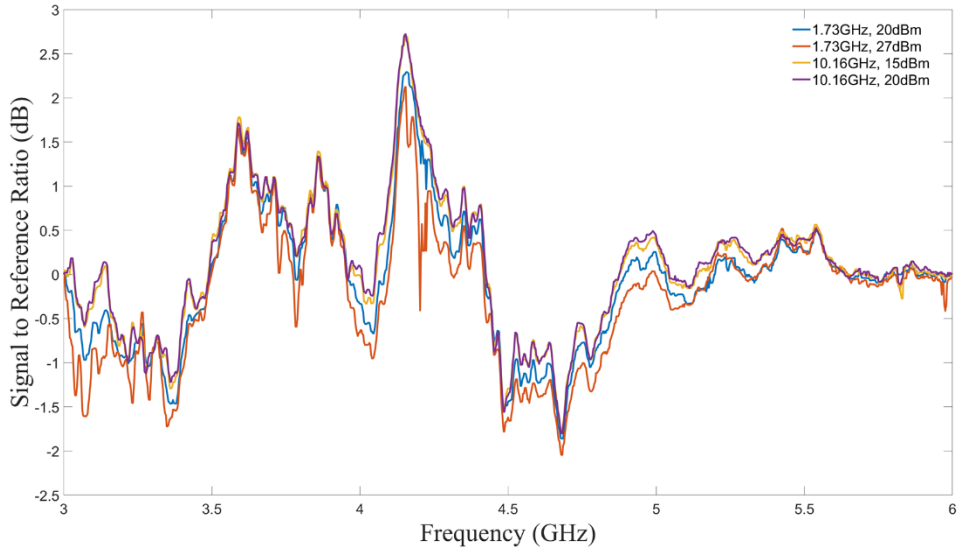

(b)

(a) Vertical Polarization (b) Horizontal Polarization

Figure 39. Signal to reference ratio

The SRR plots [Figure 39] indicates that a net emission in the predicted range of 3 GHz to 6 GHz was detected. The SRR peaked at 4.15 GHz and ranged from 2.12 dB to 2.7dB for the horizontal polarization. For the vertical polarization, the SRR peaked at 4.26

GHz and ranged from 2.05 dB to 2.29 dB. Within the SRR plot, there were instances of negative values. At these regions, the measured emissions from the metallic network exceeded the emissions from the graphene arcs.

To better understand the emitted power and device effectiveness, after accounting for system losses (cable loss, insertion loss, amplifier gain, propagation loss) [Table 5], the effective array gain based on simulated power was plotted along with the measured data [Figure 40]. Assuming coherent emission from the array, the measured power levels were consistent with an array gain of 22 dB or 150 effective units. This figure is incredibly low and represents less than $1/1000^{th}$ of the total number of fabricated devices. Even after factoring in manufacturing defects and contamination, at worst a 30% yield would be expected. Poor impedance matching would bring the yield even lower to 10%–15%.

To account for the remaining missing elements, the assumption of coherent stimulation and emission must then be considered invalid. The losses can then be explained by destructive interference. In designing the arrays, the formation of a metasurface was created unintentionally, this may have introduced a band structure commonly associated with periodic structures, which results in the low yield and the notches in the measured output spectrum. These notches are also made clear in the S_{11} plots [Figure 30].

The measured net emissions from the SRR plot [Figure 39] range from 4 GHz to 4.5 GHz, which also coincides with a valley in the S_{11} plot for the graphene wafer. From 4.5 GHz to 6 GHz the SRR assumes negative values. While the S_{11} plot can qualitatively explain this, the reference wafer assumes even lower S_{11} values over this range and should result in a much more negative SRR. Unlike an S_{11} measurement, which requires the synchronization between the stimulus and receiver as a range of frequencies are swept, this experiment did not sweep through any frequencies—only two discrete frequencies (1.73 GHz and 10.16 GHz) were applied—yet a continuum of frequencies from 4 GHz to 4.5 GHz was measured for the graphene wafer. With graphene being the only difference, this continuum of emission is due to the graphene from cyclotron radiation, effectively behaving as a band converter.

Table 5. Link budget

Component	Lower Loss (dB)	Upper Loss (dB)
Cables from PA	-3.0	-4.0
Device Insertion Loss	-0.5	-1.3
Free Space Propagation Loss (3 GHz, 6 GHz)	-35.4	-41.4
Rx Antenna Gain	6.0	6.0
Cables from Antenna to LNA	-13.0	-15.0
LNA Gain	20.0	18.0
Cables from LNA to Spectrum Analyzer	-3.0	-4.0
Total (dB)	**-28.9**	**-41.7**

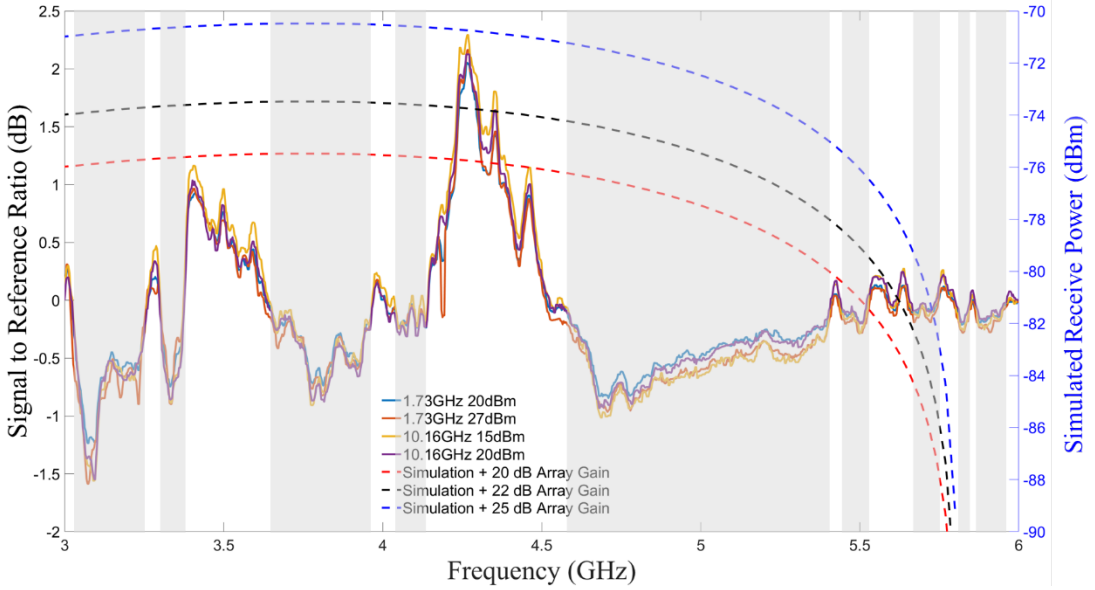

(a)

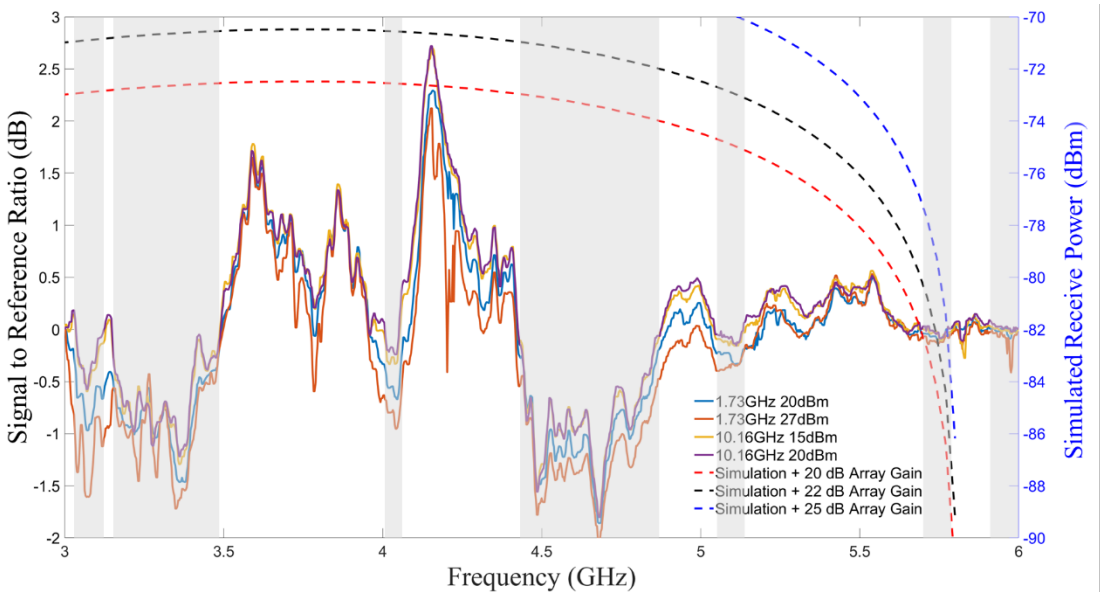

(b)

Measured data SRR (left axis) compared to simulation data (right axis). Assuming coherent emission, an array gain of 22 dB is required to meet the measured data. Notches due to band gap are highlighted in gray. (a) Vertical Polarization (b) Horizontal Polarization

Figure 40. Measurement comparison to simulation

The preceding experimental procedure and data analysis indicate that cyclotron style emissions have been produced by the graphene arcs. The emitted frequencies are consistent with the transient rotating dipole model and FE simulations. The power is also consistent with Larmor formulation and FE simulations. It was also demonstrated that the emissions were independent of the input stimulus. The shape of the emissions spectrum differed from the simulation. This was expected since array effects were not taken into account in the simulations. The array configuration was most likely creating bandgaps as highlighted in Figure 40. Some of these effects can be inferred from the S_{11} measurements [Figure 30]. The array effects on the emissions well be addressed in future work. As of this writing, this is the first known experimental demonstration of a cyclotron style emission from graphene. Given the proper scaling, arrays of these devices can be THz emitters that operate either in a source driven mode via microwave stimulus, or as a photoconductive mode with laser stimulus. As these devices were manufactured with commercially available graphene/hBN wafers, these results also indicated that the manufacturing processes and quality of these stock materials is mature enough for further deployment. This approach may help realize cost effective access to the THz spectrum.

V. NANOSCALE FABRICATION

To demonstrate the possibility of fabrication of graphene cyclotrons on nanoscale, THz arrays consisting of 100 nm and 300 nm radii were designed and fabricated. This was done using the facilities at the Center for Nanophase Materials at Oak Ridge National Laboratory (ORNL–CMNS). The device layouts and configurations were designed following the constraints of the electron beam lithography (EBL) tool (JEOL 8100 FS). Due to field of view limitations of the tool, device arrays were limited to a 1 mm x 1 mm write area. Within this constraint and setting the radius to width aspect ratio to 1, the 100 nm arc radius yielded 1.2 million devices per write area, while the 300 nm arc radius yielded 520,000 devices per write area. In theory then, the 300 nm arc radius design can emit at a frequency of 0.228 THz with a power of 8.26 μW, while the 100 nm arc radius design can emit at a frequency of 0.69 THz with a power of 24 μW.

A. FABRICATION PROCESS

The fabrication procedures were developed during 3 two-week long visits to ORNL and many trial and error attempts. The final procedure that allowed for successful fabrication of nanocyclotrons is described in the following sequence:

- Alignment layer
    - An alignment layer consisting of global alignment markers at ± 3500 μm and ± 4000 μm, and local alignment markers at the corners of each 1 mm x 1mm write area was deposited on the graphene/hBN wafer.
    - A PMMA layer was deposited by a spin coater and placed on a hot plate at 180C for 2 minutes.
    - The wafer was then placed into the JEOL 8100 FS and the alignment marker pattern was written onto the PMMA layer.
    - The wafer was developed in an MIBK/IPA 1:3 solution for 35 seconds.
    - The wafer was then subjected to a descum (low power O_2 RIE) process for 6 seconds.
    - A 5 nm layer of Cr and 50 nm layer of Au was deposited on the wafer via electron beam deposition.
    - The excess metal and PMMA were removed by a liftoff process in an acetone solution for 5 minutes with sonication.
    - Bulk graphene patterning

- A layer of NFR photoresist was deposited by spin coater and placed on a hot plate at 90°C for 90 seconds.
- The wafer was then exposed to the bulk pattern mask [Figure 41] via conventional photolithography. The bulk mask pattern consisted of a 10 x 10 array of 1 mm x 1mm squares spaced 3 mm apart centered on the wafer's origin.

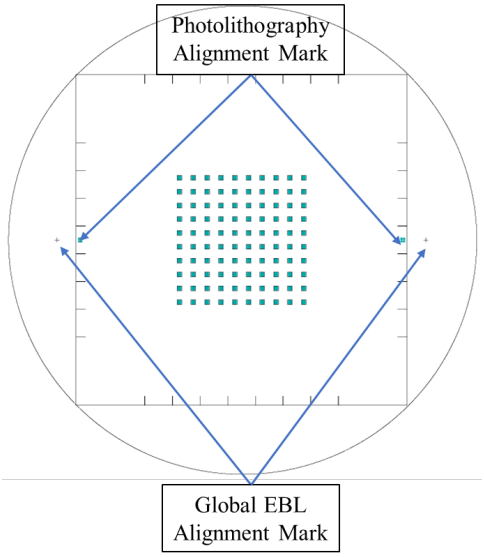

The bulk removal process removes all of the graphene on the wafer except the 1 mm × 1 mm write areas (green). Global alignment markers are located at ± 3500 µm and ± 4000 µm. Dicing marks are spaced 7 mm along the perimeter of the inscribed square.

Figure 41. Bulk graphene removal mask

- A post exposure bake at 115°C for 90 seconds was performed.
- The wafer was developed in a CD26 solution of 1 minute.
- The excess graphene was removed with a 20 second descum process.
- Excess NFR was removed in an acetone solution for 10 minutes.

- Fine graphene patterning
  - A PMMA layer was deposited by a spin coater and placed on a hot plate at 180°C for 2 minutes.
  - The wafer was then placed into the JEOL 8100 FS and the graphene arc patterns were written onto the PMMA layer.
  - The wafer was developed in an MIBK/IPA 1:3 solution for 35 seconds.
  - Excess graphene was removed with a 20 second descum process.
  - PMMA was removed in an acetone solution for 10 minutes.
- Metallic layer

- A PMMA layer was deposited by a spin coater and placed on a hot plate at 180°C for 2 minutes.
- The wafer was then placed into the JEOL 8100 FS and the metallic arc patterns were written onto the PMMA layer.
- The wafer was developed in an MIBK/IPA 1:3 solution for 35 seconds.
- The wafer was then subjected to a descum process for 6 seconds.
- A 5 nm layer of Cr and 50 nm layer of Au was deposited on the wafer via electron beam deposition.
- The excess metal and PMMA were removed by a liftoff process in an acetone solution for 5 minutes with sonication.

Figure 42 shows the resulting 300 nm x 300 nm arcs under SEM.

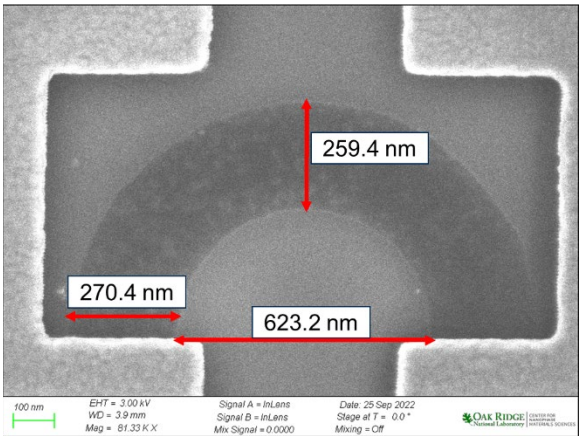

(a)

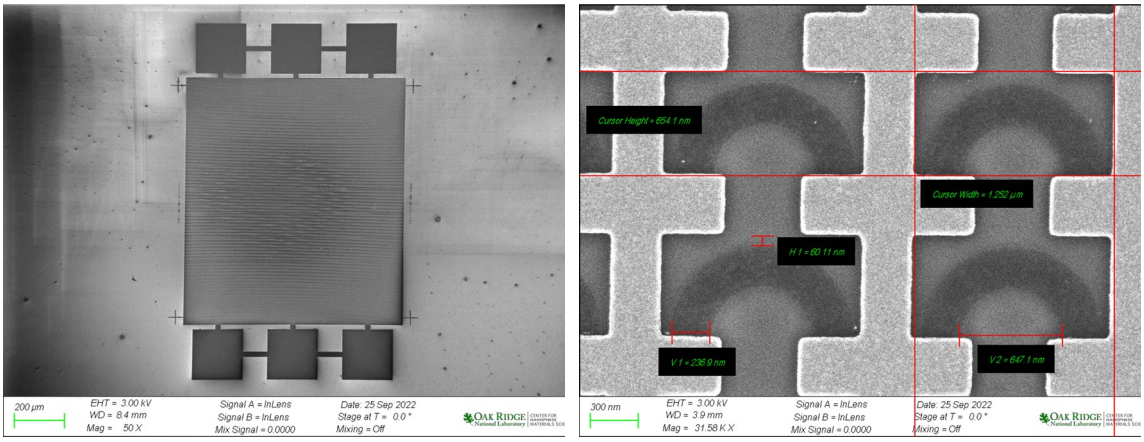

(b) (c)

(a) Single 300 nm x 300 nm arc (b) Full 1 mm x 1mm write area array (c) 2 x 2 subsection of the array

Figure 42. 300 nm x 300 nm nanoscale arrays under SEM

Figure 43 shows resulting 100 nm x 100 nm arcs under SEM.

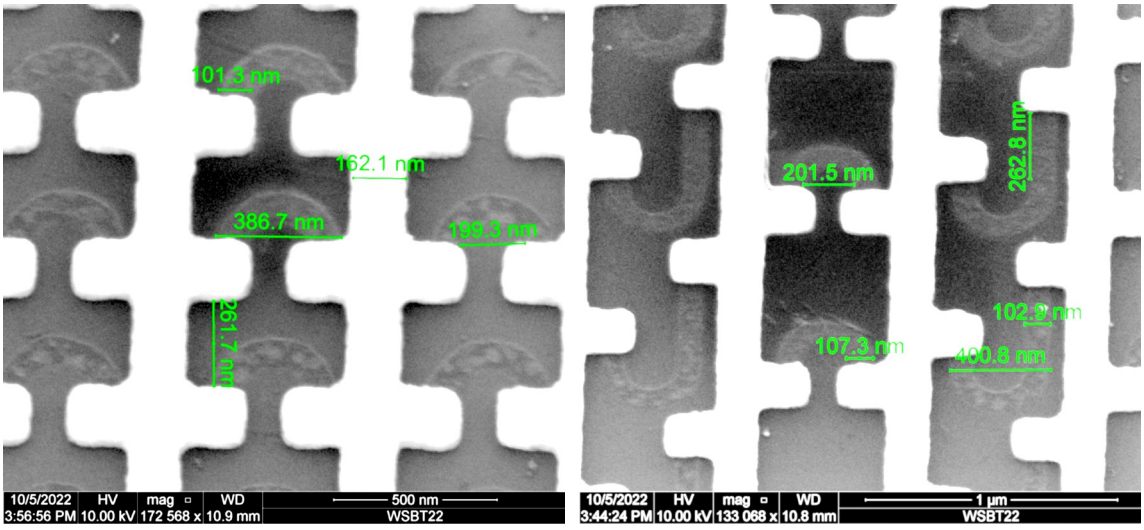

(a) (b)

(a) 100 nm x100 nm array, semicircles only (b) 100 nm x 100 nm array, with semicircles and π phase shifts.

Figure 43. 100 nm x 100 nm nanoscale arrays under SEM

B. PACKAGING

- The wafers were diced into 7 mm x 7 mm squares with a dicing saw such that a head die had a 2 x 2 array of device arrays.
- The die were then mounted onto a 28 pin CDIP with silver paste.
- The device's interface pads were then wire bonded to the terminals on the packaging.

Figure 44 shows examples of packaged nanoscale array die. These devices are to be characterized in future work.

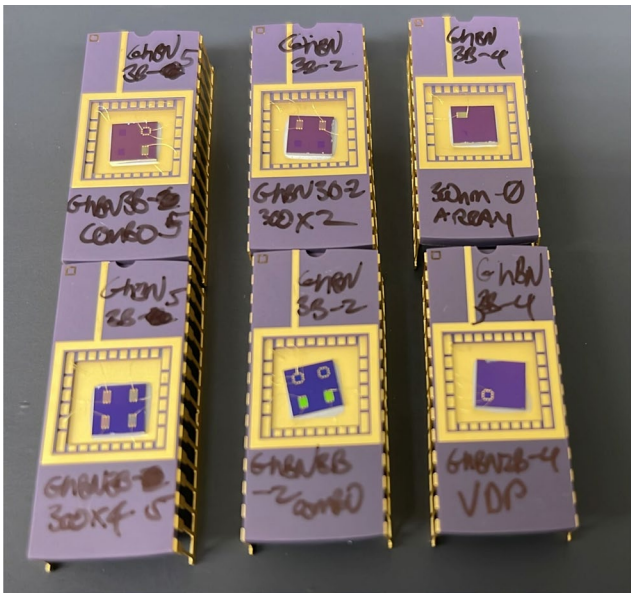

Figure 44. Packaged nanoscale array die

VI. CONCLUSIONS AND FURTHER RESEARCH DIRECTION

From this investigation, it has been determined that a solid-state cyclotron radiation device can be implemented in graphene. The characteristics of this type of device is such that the emitted frequencies are solely a function of the device's arc radius and saturation velocity of the graphene. When modeled as a rotating electric dipole, the classic result of a circular radiation pattern in the plane of orbit is demonstrated at the cyclotron frequency. Additionally, a peak emission in excess of the cyclotron frequency (ranging from 1.14 to 1.36 times the cyclotron frequency) is also emitted. The emissions were found to be independent of the stimulus frequency allowing for the device to behave as a band converter.

A fabrication feasibility study was performed on commercially procured graphene/SiO_2 and graphene/hBN/SiO_2 wafers. An assortment of features was fabricated on both types of wafers and subject to a series of characterization tests including Raman scattering, 4-point probe, and Hall effect to gain a fair comparison of the respective substrates. It was determined that commercially procured graphene on hBN best meets the quality necessary to achieve cyclotron style radiation for a scale model that operates at microwave frequencies fabricated with conventional photolithography as it was able to attain carrier mobilities comparable GaAs—a common high electron mobility semiconductor—on length scales of 1 mm.

Arrays of 10 μm arcs spanning an entire 4" graphene/hBN/SiO_2 wafer were fabricated and designed to emit in the range of 2.9 GHz to 6 GHz. Measurements detected a net emission due to the graphene in the range of 4 GHz to 4.5 GHz at powers comparable to 150 units emitting coherently. This emission and power levels held consistent even with different applied stimulus frequency and power.

Lastly, 0.228 THz and 0.69 THz arrays with arc radii of 300 nm and 100 nm respectively, were fabricated using the state-of-the-art EBL capabilities at Oak Ridge National Laboratory. A fabrication process which successfully produced the designed

arrays was formulated—thus demonstrating the possibility of fabricating large arrays, on the order of 1 million devices per square millimeter, necessary to scale the output power.

The results provide clear answers to the research questions:

- Under ideal conditions, the relation of the radius and width of the graphene arcs to output frequency and power was established. Theoretically, the limits on how high or low of a frequency that can be achieved depends only on micro- nanofabrication capabilities.
- Geometries to provide emissions in microwave and terahertz frequencies can be constructed with commercially available graphene. Some limitations due to granularity and purity are to be improved with the fast advance of the graphene manufacturing technologies.
- Cyclotron radiation was theoretically predicted and experimentally demonstrated. The power of the emissions was shown to be independent of the frequency of the emissions.

With that, the objective of this research work was achieved. With a scaled proof of concept successfully demonstrated, the opportunity for further research has been opened.

Due to the current unavailability of the in-house THz characterization equipment, THz emissions testing of the nanoscale arc arrays could not be performed at this time. Once available, testing of the nanoscale arc arrays will be performed by applying microwave sub target stimulus via the electrical interfaces on the device packaging. Stimulus over the target frequency will be provided by laser pulses, thereby operating in a photoconductive mode.

Given the calculated yield of 150 effective elements in an array of more than 100,000, the number of effective elements has room for a large improvement. Given that there are defects with the stock wafer, defects from the manufacturing process, and contamination outside of the cleanroom, the effective yield estimates should at worst be 30%. Without a total redesign, the performance of the remaining elements may be improved by integrating a matching network to the existing devices.

The arrays were designed to maximize count with redundancies, which was assumed to improve performance as well. With a proof-of-concept demonstration, a device redesign that also considers array effects such as coupling to other array elements and coupling to the metallic interconnect network needs to be done. It is also likely that due to the periodic nature of the arrays, a metasurface was inadvertently created by the metallic network which may explain deviations of the measured emission spectrum from theory and simulation. To properly design and account for this, the complexity of the simulations will greatly increase, but is a necessary step to making a more usable device.

To better understand the nature of the device behavior as part of an array versus an individual unit, simulations in future studies will include an equivalent circuit model of the device arrays. More specifically, equivalent circuit models for the metallic network and metallic network with the graphene arcs will be constructed and investigated. These models will corroborate the reflections, transmissions, and bandgaps observed in the S_{11}, S_{21}, and band conversion measurements, respectively. In addition to corroborating the measurements, the equivalent circuit models will serve as a starting point for array optimization which can be used to further tailor the emissions spectrum of the device array.

Due to the low signal-to-noise ratio of this measurement scheme, the quality of the measurements may be improved with a different testing methodology. One such method that may be particularly useful is time gated spectrum analysis. This method enables detection of signals below the noise level by applying a modulation onto the signal [81], [82]. These capabilities were not available at the time of testing.

With further development, this approach may offer cost-effective access to the THz spectrum. This work further contributes to the Navy's scientific capacity and may result in future battlespace capabilities. Cost-effective access to new spectrum such as the THz spectrum is particularly desirable for Naval applications in electronic warfare and secure communications as existing spectra is increasingly crowded during peacetime and can be contested by adversaries readily as this space is technologically mature. Results of this work may also be useful for non-destructive inspection with non-ionizing radiation of composite airframes, weapons systems, warheads, or for corrosion detection of ship hulls.

THIS PAGE INTENTIONALLY LEFT BLANK

SUPPLEMENTAL

FEM SOFTWARE CONFIGURATION

This thesis includes a supplemental document with frame grabs from the commercial software package COMSOL Multiphysics, which was used for the FEM simulations. The frame grabs detail the model parameters, boundary conditions, and equations for the simulations in Chapter II. Please contact the Dudley Knox Library at the Naval Postgraduate School for more information.

THIS PAGE INTENTIONALLY LEFT BLANK

LIST OF REFERENCES

[1] H.-J. Song and T. Nagatsuma, "Present and Future of Terahertz Communications," *IEEE Trans. Terahertz Sci. Technol.*, vol. 1, no. 1, pp. 256–263, Sep. 2011, Available: https://doi.org/10.1109/TTHZ.2011.2159552

[2] R. I. Stantchev *et al.*, "Noninvasive, near-field terahertz imaging of hidden objects using a single-pixel detector," *Sci. Adv.*, vol. 2, no. 6, p. e1600190, Jun. 2016, Available: https://doi.org/10.1126/sciadv.1600190

[3] C. M. Armstrong, "The Truth About Terahertz," *IEEE Spectrum*, Aug. 17, 2012 [Online]. Available: http://spectrum.ieee.org/aerospace/military/the-truth-about-terahertz

[4] K. S. Novoselov, "Electric Field Effect in Atomically Thin Carbon Films," *Science*, vol. 306, no. 5696, pp. 666–669, Oct. 2004, Available: https://doi.org/10.1126/science.1102896

[5] K. S. Novoselov *et al.*, "Two-dimensional atomic crystals," *Proc. Natl. Acad. Sci.*, vol. 102, no. 30, pp. 10451–10453, Jul. 2005, Available: https://doi.org/10.1073/pnas.0502848102

[6] A. C. Ferrari *et al.*, "Raman Spectrum of Graphene and Graphene Layers," *Phys. Rev. Lett.*, vol. 97, no. 18, Oct. 2006, Available: https://doi.org/10.1103/PhysRevLett.97.187401

[7] A. K. Geim and A. H. MacDonald, "Graphene: Exploring carbon flatland," *Phys. Today*, vol. 60, no. 8, pp. 35–41, Aug. 2007, Available: https://doi.org/10.1063/1.2774096

[8] K. S. Novoselov *et al.*, "Two-dimensional gas of massless Dirac fermions in graphene," *Nature*, vol. 438, no. 7065, pp. 197–200, Nov. 2005, Available: https://doi.org/10.1038/nature04233

[9] M. C. Lemme, T. J. Echtermeyer, M. Baus, and H. Kurz, "A Graphene Field-Effect Device," *IEEE Electron Device Lett.*, vol. 28, no. 4, pp. 282–284, Apr. 2007, Available: https://doi.org/10.1109/LED.2007.891668

[10] Y. Wu, M. Qu, and Y. Liu, "A Generalized Lossy Transmission-Line Model for Tunable Graphene-Based Transmission Lines with Attenuation Phenomenon," *Sci. Rep.*, vol. 6, no. 1, p. 31760, Aug. 2016, Available: https://doi.org/10.1038/srep31760

[11] A. Y. Nikitin, F. Guinea, F. J. Garcia-Vidal, and L. Martin-Moreno, "Edge and waveguide terahertz surface plasmon modes in graphene microribbons," *Phys. Rev. B*, vol. 84, no. 16, Oct. 2011, Available: https://doi.org/10.1103/PhysRevB.84.161407

[12] J. Perruisseau-Carrier, "Graphene for antenna applications: Opportunities and challenges from microwaves to THz," *2012 Loughb. Antennas Propag. Conf. LAPC*, Nov. 2012, Available: https://doi.org/10.1109/LAPC.2012.6402934

[13] Y. Yao *et al.*, "Broad Electrical Tuning of Graphene-Loaded Plasmonic Antennas," *Nano Lett.*, vol. 13, no. 3, pp. 1257–1264, Feb. 2013, Available: https://doi.org/10.1021/nl3047943

[14] W.-K. Tse, E. H. Hwang, and S. D. Sarma, "Ballistic hot electron transport in graphene," *Appl. Phys. Lett.*, vol. 93, no. 2, p. 023128, Jul. 2008, Available: https://doi.org/10.1063/1.2956669

[15] R. S. Shishir and D. K. Ferry, "Velocity saturation in intrinsic graphene," *J. Phys. Condens. Matter*, vol. 21, no. 34, p. 344201, Jul. 2009, Available: https://doi.org/10.1088/0953-8984/21/34/344201

[16] K. Tantiwanichapan, X. Wang, A. K. Swan, and R. Paiella, "Graphene on nanoscale gratings: a novel materials platform for THz electron-beam radiation," in *Advanced Photonics 2015*, Optical Society of America, 2015, p. IM4A.2. Available: https://doi.org/10.1364/IPRSN.2015.IM4A.2

[17] F. Anwar, C. R. Carlos, V. Saraswat, V. S. Mangu, M. S. Arnold, and F. Cavallo, "Nanoscale graphene/Ge wigglers as building blocks for THz sources," *AIP Adv.*, vol. 7, no. 11, p. 115015, Nov. 2017, Available: https://doi.org/10.1063/1.4986513

[18] H. Ito, "Breakthroughs in Photonics 2013: Terahertz Wave Photonics," *IEEE Photonics J.*, vol. 6, no. 2, pp. 1–5, Apr. 2014, Available: https://doi.org/10.1109/JPHOT.2014.2309648

[19] M. Levinshtein, S. Rumyantsev, and M. Shur, *Handbook Series on Semiconductor Parameters: Volume 1: Si, Ge, C (Diamond), GaAs, GaP, GaSb, InAs, InP, InSb*, vol. 1. WORLD SCIENTIFIC, 1996. Available: https://doi.org/10.1142/2046-vol1

[20] A. Dargys and J. Kundrotas, *Handbook on physical properties of Ge, Si, GaAs and InP*. Vilnius, Lithuania: Science and Encyclopedia Publishers, 1994.

[21] D. W. Palmer, "PROPERTIES OF THE III-V COMPOUND SEMICONDUCTORS," Feb. 2006 [Online]. Available: www.semiconductors.co.uk

[22] D. A. Neamen, *Semiconductor physics and devices: basic principles*, 4th ed. New York, NY: McGraw-Hill, 2012.

[23] J.-E. Muller *et al.*, "A GaAs HEMT MMIC chip set for automotive radar systems fabricated by optical stepper lithography," in *GaAs IC Symposium IEEE Gallium Arsenide Integrated Circuit Symposium. 18th Annual Technical Digest 1996*, Orlando, FL, USA: IEEE, 1996, pp. 189–192. Available: https://doi.org/10.1109/GAAS.1996.567866

[24] D.-H. Kim and J. A. Del Alamo, "Scalability of Sub-100 nm InAs HEMTs on InP Substrate for Future Logic Applications," *IEEE Trans. Electron Devices*, vol. 57, no. 7, pp. 1504–1511, Jul. 2010, Available: https://doi.org/10.1109/TED.2010.2049075

[25] W. R. Deal, K. Leong, A. Zamora, V. Radisic, and X. B. Mei, "Recent progress in scaling InP HEMT TMIC technology to 850 GHz," in *2014 IEEE MTT-S International Microwave Symposium (IMS2014)*, Tampa, FL, USA: IEEE, Jun. 2014, pp. 1–3. Available: https://doi.org/10.1109/MWSYM.2014.6848588

[26] *High_Electron_MobilityTransistor_-_electron_energy_band_structure_(DE).svg: Cepheiden derivative work: sfu* [Online]. Available: https://upload.wikimedia.org/wikipedia/commons/9/9e/HEMT-band_structure_scheme-en.svg

[27] K. Saito, T. Tanabe, and Y. Oyama, "Design of a GaP/Si composite waveguide for CW terahertz wave generation via difference frequency mixing," *Appl. Opt.*, vol. 53, no. 17, p. 3587, Jun. 2014, Available: https://doi.org/10.1364/AO.53.003587

[28] K. Saito, T. Tanabe, and Y. Oyama, "Widely tunable surface-emitted monochromatic terahertz-wave generation beyond the Reststrahlen band," *Opt. Commun.*, vol. 335, pp. 99–101, Jan. 2015, Available: https://doi.org/10.1016/j.optcom.2014.09.013

[29] S.-H. Yang, M. R. Hashemi, C. W. Berry, and M. Jarrahi, "7.5% Optical-to-Terahertz Conversion Efficiency Offered by Photoconductive Emitters With Three-Dimensional Plasmonic Contact Electrodes," *IEEE Trans. Terahertz Sci. Technol.*, vol. 4, no. 5, pp. 575–581, Sep. 2014, Available: https://doi.org/10.1109/TTHZ.2014.2342505

[30] G. C. Loata, M. D. Thomson, T. Löffler, and H. G. Roskos, "Radiation field screening in photoconductive antennae studied via pulsed terahertz emission spectroscopy," *Appl. Phys. Lett.*, vol. 91, no. 23, p. 232506, Dec. 2007, Available: https://doi.org/10.1063/1.2823590

[31] C. W. Berry, M. R. Hashemi, and M. Jarrahi, "Generation of high power pulsed terahertz radiation using a plasmonic photoconductive emitter array with logarithmic spiral antennas," *Appl. Phys. Lett.*, vol. 104, no. 8, p. 081122, Feb. 2014, Available: https://doi.org/10.1063/1.4866807

[32] R. Köhler *et al.*, "Terahertz semiconductor-heterostructure laser," *Nature*, vol. 417, no. 6885, pp. 156–159, May 2002, Available: https://doi.org/10.1038/417156a

[33] I. Waldmueller, M. C. Wanke, and W. W. Chow, "Circumventing the Manley-Rowe Quantum Efficiency Limit in an Optically Pumped Terahertz Quantum-Cascade Amplifier," *Phys. Rev. Lett.*, vol. 99, no. 11, p. 117401, Sep. 2007, Available: https://doi.org/10.1103/PhysRevLett.99.117401

[34] J. D. Jackson, *Classical electrodynamics*, 3rd ed. New York: Wiley, 1999.

[35] S. Zaremba and W. Kleeven, "Cyclotrons: Magnetic Design and Beam Dynamics," *CERN Yellow Rep. Sch. Proc.*, p. 177 Pages, Jun. 2017, Available: https://doi.org/10.23730/CYRSP-2017-001.177

[36] A. Einstein, "Zur Elektrodynamik bewegter Körper," *Ann. Phys.*, vol. 322, no. 10, pp. 891–921, 1905, Available: https://doi.org/10.1002/andp.19053221004

[37] C. K. Ullal, J. Shi, and R. Sundararaman, "Electron mobility in graphene without invoking the Dirac equation," *Am. J. Phys.*, vol. 87, no. 4, pp. 291–295, Apr. 2019, Available: https://doi.org/10.1119/1.5092453

[38] L. Landau, "Diamagnetismus der Metalle," *Z. Phys.*, vol. 64, no. 9–10, pp. 629–637, Sep. 1930, Available: https://doi.org/10.1007/BF01397213

[39] T. Morimoto, Y. Hatsugai, and H. Aoki, "Cyclotron radiation and emission in graphene," *Phys Rev B*, vol. 78, no. 7, p. 073406, Aug. 2008, Available: https://doi.org/10.1103/PhysRevB.78.073406

[40] R. Jago, T. Winzer, A. Knorr, and E. Malic, "Graphene as gain medium for broadband lasers," *Phys Rev B*, vol. 92, no. 8, p. 085407, Aug. 2015, Available: https://doi.org/10.1103/PhysRevB.92.085407

[41] N. Cole and T. M. A. Jr, "Cyclotron Resonance Gain for FIR and THz Radiation in Graphene." 2017.

[42] V. E. Dorgan, M.-H. Bae, and E. Pop, "Mobility and saturation velocity in graphene on SiO2," *Appl. Phys. Lett.*, vol. 97, no. 8, p. 082112, Aug. 2010, Available: https://doi.org/10.1063/1.3483130

[43] A. Reina *et al.*, "Large Area, Few-Layer Graphene Films on Arbitrary Substrates by Chemical Vapor Deposition," *Nano Lett.*, vol. 9, no. 1, pp. 30–35, 2009, Available: https://doi.org/10.1021/nl801827v

[44] R. Kitaura *et al.*, "Chemical Vapor Deposition Growth of Graphene and Related Materials," *J. Phys. Soc. Jpn.*, vol. 84, no. 12, p. 121013, Dec. 2015, Available: https://doi.org/10.7566/jpsj.84.121013

[45] D. De Fazio *et al.*, "High-Mobility, Wet-Transferred Graphene Grown by Chemical Vapor Deposition," *ACS Nano*, vol. 13, no. 8, pp. 8926–8935, 2019, Available: https://doi.org/10.1021/acsnano.9b02621

[46] M. Wojtaszek, "Graphene: a two type charge carrier system," University of Groningen, Groningen, NL, 2009 [Online]. Available: https://www.rug.nl/research/zernike/education/topmasternanoscience/ns201wojtaszek.pdf

[47] K. Tantiwanichapan, X. Wang, A. K. Swan, and R. Paiella, "Graphene on nanoscale gratings for the generation of terahertz Smith-Purcell radiation," *Appl. Phys. Lett.*, vol. 105, no. 24, p. 241102, Dec. 2014, Available: https://doi.org/10.1063/1.4904264

[48] I. Kaminer *et al.*, "Efficient plasmonic emission by the quantum Čerenkov effect from hot carriers in graphene," *Nat. Commun.*, vol. 7, no. 1, p. ncomms11880, Jun. 2016, Available: https://doi.org/10.1038/ncomms11880

[49] Y. Li, K. Tantiwanichapan, A. K. Swan, and R. Paiella, "Graphene plasmonic devices for terahertz optoelectronics," *Nanophotonics*, vol. 9, no. 7, pp. 1901–1920, Jul. 2020, Available: https://doi.org/10.1515/nanoph-2020-0211

[50] J. Planillo and F. Alves, "Design and modeling of a planar graphene structure as a terahertz cyclotron radiation source," *Sci. Rep.*, vol. 11, no. 1, p. 15965, Aug. 2021, Available: https://doi.org/10.1038/s41598-021-95502-9

[51] CheapTubesInc., "Product Specifications: CVD Graphene On Si-SiO2 4inch." https://www.cheaptubes.com/product/cvd-graphene-si-sio2-4inch/

[52] C. L. Gardner, "Numerical simulation of a steady-state electron shock wave in a submicrometer semiconductor device," *IEEE Trans. Electron Devices*, vol. 38, no. 2, pp. 392–398, 1991, Available: https://doi.org/10.1109/16.69922

[53] S. A. Kozlov, A. M. Oparin, and V. M. Chechetkin, "Numerical simulation of the process of formation of shock waves in electron gas in a field-effect transistor," *Comput. Math. Math. Phys.*, vol. 49, no. 12, pp. 2149–2157, Dec. 2009, Available: https://doi.org/10.1134/S0965542509120136

[54] C. Kunz, "Synchrotron radiation," *Meet. Technol. Aris. High-Energy Phys.*, pp. 155–166, 1974, Available: http://dx.doi.org/10.5170/CERN-1974-009-V-1.155

[55] D. J. Griffiths, *Introduction to Electrodynamics*. Pearson, 2013.

[56] M. Y. Han, B. Özyilmaz, Y. Zhang, and P. Kim, "Energy Band-Gap Engineering of Graphene Nanoribbons," *Phys. Rev. Lett.*, vol. 98, no. 20, May 2007, Available: https://doi.org/10.1103/PhysRevLett.98.206805

[57] M. C. Lemme *et al.*, "Etching of Graphene Devices with a Helium Ion Beam," *ACS Nano*, vol. 3, no. 9, pp. 2674–2676, Sep. 2009, Available: https://doi.org/10.1021/nn900744z

[58] J.-H. Chen, C. Jang, S. Xiao, M. Ishigami, and M. S. Fuhrer, "Intrinsic and extrinsic performance limits of graphene devices on SiO2," *Nat. Nanotechnol.*, vol. 3, no. 4, pp. 206–209, Mar. 2008, Available: https://doi.org/10.1038/nnano.2008.58

[59] M. P. Legua, I. Morales, and L. M. Sánchez Ruiz, "The Heaviside Step Function and MATLAB," in *Computational Science and Its Applications – ICCSA 2008*, O. Gervasi, B. Murgante, A. Laganà, D. Taniar, Y. Mun, and M. L. Gavrilova, Eds., in Lecture Notes in Computer Science, vol. 5072. Berlin, Heidelberg: Springer Berlin Heidelberg, 2008, pp. 1212–1221. Available: https://doi.org/10.1007/978-3-540-69839-5_93

[60] J. Planillo and F. Alves, "Fabrication and Characterization of Micrometer Scale Graphene Structures for Large-Scale Ultra-Thin Electronics," *Electronics*, vol. 11, no. 5, p. 752, Mar. 2022, Available: https://doi.org/10.3390/electronics11050752

[61] S. J. Chae *et al.*, "Synthesis of large-area graphene layers on poly-nickel substrate by chemical vapor deposition: Wrinkle formation," *Adv Mater*, vol. 21, no. 22, pp. 2328–2333, Jun. 2009.

[62] S. Bae *et al.*, "Roll-to-roll production of 30-inch graphene films for transparent electrodes," *Nat Nanotechnol*, vol. 5, no. 8, pp. 574–578, Aug. 2010.

[63] S. Majety *et al.*, "Semiconducting hexagonal boron nitride for deep ultraviolet photonics," *Quantum Sens. Nanophotonic Devices IX*, Jan. 2012, Available: https://doi.org/10.1117/12.914084

[64] A. G. F. Garcia *et al.*, "Effective Cleaning of Hexagonal Boron Nitride for Graphene Devices," *Nano Lett.*, vol. 12, no. 9, pp. 4449–4454, 2012, Available: https://doi.org/10.1021/nl3011726

[65] K. K. Kim, S. M. Kim, and Y. H. Lee, "A new horizon for hexagonal boron nitride film," *J. Korean Phys. Soc.*, vol. 64, no. 10, pp. 1605–1616, May 2014, Available: https://doi.org/10.3938/jkps.64.1605

[66] M. A. Yamoah, W. Yang, E. Pop, and D. Goldhaber-Gordon, "High-Velocity Saturation in Graphene Encapsulated by Hexagonal Boron Nitride," *ACS Nano*, vol. 11, no. 10, pp. 9914–9919, 2017, Available: https://doi.org/10.1021/acsnano.7b03878

[67] S. M. Kim *et al.*, "Synthesis of Patched or Stacked Graphene and hBN Flakes: A Route to Hybrid Structure Discovery," *Nano Lett.*, vol. 13, no. 3, pp. 933–941, Mar. 2013, Available: https://doi.org/10.1021/nl303760m

[68] Y. Stehle *et al.*, "Synthesis of Hexagonal Boron Nitride Monolayer: Control of Nucleation and Crystal Morphology," *Chem. Mater.*, vol. 27, no. 23, pp. 8041–8047, Nov. 2015, Available: https://doi.org/10.1021/acs.chemmater.5b03607

[69] J. Y. Kim *et al.*, "Graphene Electrode Enabling Electrochromic Approaches for Daylight-Dimming Applications," *Sci. Rep.*, vol. 8, no. 1, Mar. 2018, Available: https://doi.org/10.1038/s41598-018-22274-0

[70] Y. Woo, "Transparent Conductive Electrodes Based on Graphene-Related Materials," *Micromachines*, vol. 10, no. 1, p. 13, Dec. 2018, Available: https://doi.org/10.3390/mi10010013

[71] I. Childres, L. A. Jauregui, W. Park, H. Cao, Y. P. Chen, and others, "Raman spectroscopy of graphene and related materials," *New Dev. Photon Mater. Res.*, vol. 1, pp. 1–20, 2013.

[72] D. R. Young, E. A. Irene, D. J. DiMaria, R. F. De Keersmaecker, and H. Z. Massoud, "Electron trapping in SiO2 at 295 and 77 °K," *J. Appl. Phys.*, vol. 50, no. 10, pp. 6366–6372, Oct. 1979, Available: https://doi.org/10.1063/1.325727

[73] B. J. van Wees *et al.*, "Quantized conductance of point contacts in a two-dimensional electron gas," *Phys. Rev. Lett.*, vol. 60, no. 9, pp. 848–850, Feb. 1988, Available: https://doi.org/10.1103/physrevlett.60.848

[74] Y. X. Hui, N. An, K. Chen, X. J. Li, W. L. Li, and Z. Y. Ren, "Research on Hall Effect of Graphene by Var Der Pauw Method," *Adv. Mater. Res.*, vol. 1120–1121, pp. 383–387, Jul. 2015, Available: https://doi.org/10.4028/www.scientific.net/amr.1120-1121.383

[75] L. Banszerus *et al.*, "Extraordinary high room-temperature carrier mobility in graphene-WSe_2 heterostructures." 2019.

[76] S. Sze and J. Irvin, "Resistivity, mobility and impurity levels in GaAs, Ge, and Si at 300 K," *Solid-State Electron.*, vol. 11, no. 6, pp. 599–602, 1968.

[77] C. R. Dean *et al.*, "Boron nitride substrates for high-quality graphene electronics," *Nat. Nanotechnol.*, vol. 5, no. 10, pp. 722–726, Oct. 2010, Available: https://doi.org/10.1038/nnano.2010.172

[78] Y. Khatami, H. Li, C. Xu, and K. Banerjee, "Metal-to-Multilayer-Graphene Contact—Part I: Contact Resistance Modeling," *IEEE Trans. Electron Devices*, vol. 59, no. 9, pp. 2444–2452, Sep. 2012, Available: https://doi.org/10.1109/TED.2012.2205256

[79] Y. Khatami, H. Li, C. Xu, and K. Banerjee, "Metal-to-Multilayer-Graphene Contact—Part II: Analysis of Contact Resistance," *IEEE Trans. Electron Devices*, vol. 59, no. 9, pp. 2453–2460, Sep. 2012, Available: https://doi.org/10.1109/TED.2012.2205257

[80] J. T. Smith, A. D. Franklin, D. B. Farmer, and C. D. Dimitrakopoulos, "Reducing Contact Resistance in Graphene Devices through Contact Area Patterning," *ACS Nano*, vol. 7, no. 4, pp. 3661–3667, Apr. 2013, Available: https://doi.org/10.1021/nn400671z

[81] R. H. Dicke and R. H. Romer, "Pulse Techniques in Microwave Spectroscopy," *Rev. Sci. Instrum.*, vol. 26, no. 10, pp. 915–928, Oct. 1955, Available: https://doi.org/10.1063/1.1715156

[82] Keysight Technologies, "Spectrum Analysis Basics." Keysight Technologies, Dec. 16, 2020 [Online]. Available: https://www.keysight.com/us/en/assets/7018-06714/application-notes/5952-0292.pdf

INITIAL DISTRIBUTION LIST

1. Defense Technical Information Center
   Ft. Belvoir, Virginia

2. Dudley Knox Library
   Naval Postgraduate School
   Monterey, California